Model-based analysis of solute transport and potential carbon mineralization in a permafrost catchment under seasonal variability and climate change

Alexandra Hamm [1,2], Erik Schytt Mannerfelt [3], Aaron A. Mohammed [4,5], Scott L. Painter [6], Ethan T. Coon [6], and Andrew Frampton [1,2]

[1]Department of Physical Geography, Stockholm University, Stockholm ,Sweden
[2]Bolin Centre for Climate Research, Stockholm University, Stockholm, Sweden
[3]Department of Geosciences, University of Oslo, Oslo, Norway
[4]Department of Earth and Environmental Sciences, Syracuse University, New York, 13244, USA
[5]Department of Civil and Environmental Engineering, Syracuse University, New York, 13244, USA
[6]Climate Change Science Institute and Environmental Sciences Division, Oak Ridge National Laboratory, Oak Ridge, Tennessee 37830, USA

Correspondence: Alexandra Hamm (alexandra.hamm@natgeo.su.se)

Abstract. Permafrost carbon, stored in frozen organic matter across vast Arctic and sub-Arctic regions, represents a substantial and increasingly vulnerable carbon reservoir. As global temperatures rise, the accelerated thawing of permafrost releases greenhouse gases, exacerbating climate change. However, freshly thawed permafrost carbon may also experience lateral transport by groundwater flow to surface water recipients such as rivers and lakes, increasing the terrestrial-to-aquatic transfer of permafrost carbon. The mobilization and subsurface transport mechanisms are poorly understood and not accounted for in global climate models, leading to high uncertainties in the predictions of the permafrost carbon feedback. Here, we focus on a sub-catchment in Endalen, Svalbard, as a representative example of a high Arctic hillslope underlain by continuous permafrost. We analyze solute transport in the form of a non-reactive tracer representing dissolved organic carbon (DOC) using a physics-based numerical model with the objective to study governing cryotic and hydrodynamic transport mechanisms relevant for warming permafrost regions. We first analyze transport times for DOC pools at different locations within the active layer under present-day climatic conditions and proceed to study susceptibility for deeper ancient carbon release in the upper permafrost due to thaw under different warming scenarios. Results suggest that DOC in the active layer near the permafrost table experiences rapid lateral transport upon thaw due to saturated conditions and lateral flow, while DOC close to the ground surface experiences slower transport due flow in unsaturated soil. Deeper permafrost carbon release exhibits vastly different transport behaviors depending on warming and thaw rate. Gradual warming leads to small fractions of DOC being mobilized every year, while the majority moves vertically through percolation and cryosuction. Abrupt thaw resulting from a single very warm year leads to faster lateral transport times, similar to active layer DOC released in saturated conditions. Lastly, we analyze the potential susceptibility of DOC to mineralization to CO_2 prior to export due to soil moisture and temperature conditions. We find that high liquid saturation during transport coincides with very low mineralization rates and potentially inhibits mineralization

into CO_2 before export. Overall, the results highlight the importance of subsurface hydrologic and thermal conditions on the retention and lateral export of permafrost carbon by subsurface flow.

1   Introduction

Permafrost stores vast amounts of soil organic carbon (SOC) currently immobilized in frozen ground (Zimov et al., 2006). This carbon stock has been built up over millennia and is not currently part of the active carbon cycle, but is subject to remobilization under climate change (Tarnocai et al., 2009). Due to climate warming and permafrost loss, this carbon gets mobilized when thawed out (Miner et al., 2022), which may lead to the possible release of large amounts of terrestrial carbon into the atmosphere in the form of greenhouse gases (GHGs). However, the fate of the mobilized carbon is fraught with uncertainty around the questions of how much of this carbon will ultimately be released to the atmosphere and how much of it experiences lateral waterborne transport. Given that permafrost soils currently contain twice the amount of carbon compared to the present atmospheric CO_2, the potential release of this vast carbon stock into the atmosphere would exert a profound impact on global climate dynamics (e.g., Schuur et al., 2015).

Apart from vertical release as GHGs through microbial mineralization, newly thawed carbon can also be dissolved in groundwater and then be transported as dissolved organic carbon (DOC, Connolly et al., 2020) and lead to a lateral export of permafrost carbon. This lateral transport increases the terrestrial-to-aquatic transfer of SOC, which affects rivers and oceans. Depending on its biogdegradability, a large part of riverine DOC will be mineralized in the river or delivered to oceans, a small part can be buried within the river sediments (Cole et al., 2007; O'Donnell et al., 2012; Abbott et al., 2014). The fate of permafrost carbon is an essential piece of the global carbon cycle and requires a better understanding of DOC transport mechanics in groundwater (Plaza et al., 2019).

Thawing of permafrost not only releases organic carbon but also has implications for the mobilization of other chemical species, including contaminants such as mercury or trace metals. As permafrost thaws, the previously sequestered contaminants in frozen soil can be released into the environment, potentially increasing pollutant levels in aquatic systems, threatening human health (O'Donnell et al., 2012; Smith et al., 2024). Additionally, the increased input of DOC from thawed permafrost can influence surface water chemistry. The lateral transport of DOC into oceans may interact with ocean acidification processes, as increased CO_2 absorption by oceans decreases pH (Semiletov et al., 2016). This interaction could affect marine biogeochemical processes and ecosystem health.

Groundwater flow in permafrost regions is for the most part restricted to sub- and supra-permafrost groundwater flow (Walvoord and Kurylyk, 2016). With permafrost acting as a largely impermeable layer between the two, shallow and deep aquifers are mostly disconnected systems in continuous permafrost regions (e.g., Kane et al., 2013). Most of permafrost carbon in the circumpolar permafrost region (46% of SOC in the upper three meters) is stored in the uppermost meter of permafrost soils with deeper layers (1–2 m and 2–3 m depth) containing increasingly less carbon (34% and 20% of total SOC in the upper three meters, respectively Hugelius et al., 2014). Within the active layer, a higher density of carbon abundance can be observed close to the surface in the top organic layer (TOL) as well as cryoturbated material close to the active layer-permafrost boundary (Siewert et al., 2015).

Lateral transport of compounds in permafrost regions is not only important for the fate of organic carbon, but also for the transport of anthropogenic contaminants (Miner et al., 2021), mercury bound to organic material (Schuster et al., 2018), and other chemical species (Wu et al., 2022). Observing transport and groundwater flow in general is inherently difficult; field experiments in which tracers are used in permafrost landscapes (e.g., Wales et al., 2020) give an idea of the velocity of flow as well as the dispersion of solutes but lack the possibility to obtain observations continuous in time. Numerical models allow both simulating current groundwater flow as well as associated heat and solute transport (e.g., McKenzie et al., 2007; Frampton et al., 2011; Harp et al., 2016; Lamontagne-Hallé et al., 2018; Dagenais et al., 2020; Sjöberg et al., 2021), and also enable future predictions and changes in the cryotic-hydrological system (e.g., Bense et al., 2009; Ge et al., 2011; Bense et al., 2012; Frampton et al., 2013; Frampton and Destouni, 2015; Kurylyk et al., 2016; Shojae Ghias et al., 2019; Painter et al., 2023). Therefore, modeling constitutes an important tool for investigating the ultimate fate of permafrost carbon.

Numerical modeling of solute transport under freeze-thaw conditions is computationally challenging and requires well-optimized computer code that can solve the complex interplay between thawing, freezing, groundwater flow, and solute transport (Lapalme et al., 2023; Lemieux et al., 2024). Recent modeling results have highlighted the importance of including freeze-thaw processes when modeling solute transport in permafrost regions (Frampton et al., 2011; Mohammed et al., 2021; Guimond et al., 2021; Huang and Rudolph, 2023; Zastruzny et al., 2024). Jafarov et al. (2022) used the Advanced Terrestrial Simulator (ATS, Coon et al., 2019) to show the difference between including and excluding freeze-thaw dynamics in simulations representing low centered polygons in a polygonal tundra landscape. They use a non-reactive tracer to represent dissolved constituents in the groundwater and found that in the simulations including freeze-thaw, most of the modeled tracer gets mobilized within the freeze-up period and vertical tracer movement is greatly enhanced as compared to the simulations that do not account for freeze-thaw dynamics, where lateral transport is significantly lower. They suggest that capillary forces (cryosuction) might play a substantial role in the movement of solutes during freeze-up.

In this study, we quantify conservative solute transport in the active layer along a high Arctic hillslope system in Endalen, Svalbard, underlain by continuous permafrost. We analyze non-reactive advective transport by simulating waterborne transport of a tracer as a proxy for DOC (Fig. 1a), without accounting for carbon-specific reactions. We define multiple tracers that represent carbon pools in different depths in the active layer as well as within the permafrost (Fig. 1b). Carbon pools in the contemporary active layer are represented by TOL carbon close to the surface (seasonal plant litter) and buried carbon (cryoturbated carbon) at the bottom of the active layer. We analyze the importance of these sources by comparing the difference
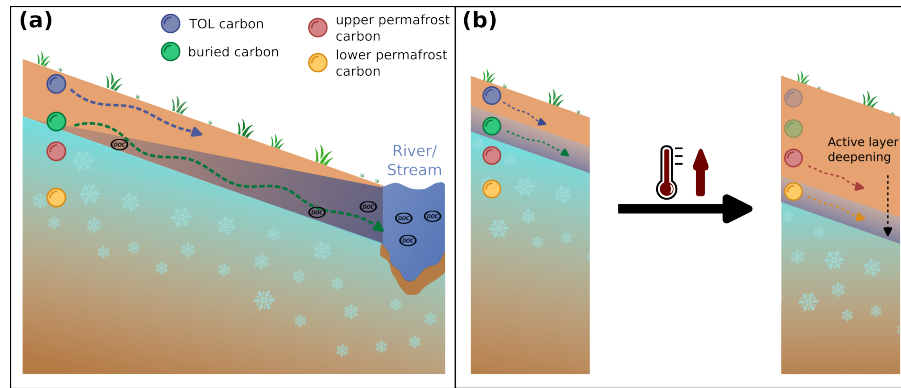
Figure 1. Conceptual representation of permafrost carbon transport in the form of dissolved organic carbon in a High Arctic hillslope setting underlain by continuous permafrost. (**a**) Different carbon pools in the active layer (Top organic layer, TOL) carbon, blue sphere, and buried carbon, green sphere) represent present-day active layer carbon release with hypothesized differences in transport velocities indicated by the length of the arrow (short: slow, long: fast). (**b**) Ancient carbon (red and yellow spheres) represent carbon sources within the permafrost, currently immobilized, and their mobilization upon permafrost thaw through increasing air temperatures in the course of climate change and associated active layer deepening.

in transport velocities, which translates to residence time in the unfrozen soil and availability for microbial mineralization that can then lead to the release of GHGs. Furthermore, we explore the effect of a warming climate on mobilization of ancient, currently frozen, carbon in the upper permafrost layers. Two additional tracers in the model represent carbon sources that are presently immobilized in permafrost but susceptible to release by active layer expansion due to warming. We hypothesize that for a high-Arctic hillslope as represented by our study site in Endalen, Svalbard (i) buried carbon within the active layer will be transported faster than TOL carbon due to higher saturated soil conditions at the bottom of the active layer; and (ii) ancient permafrost carbon will be exposed to similar highly saturated late season conditions leading to rapid transport upon thaw. This insight into transport mechanisms active in permafrost landscapes will contribute to the understanding of the impacts of hydrological flows on the permafrost carbon feedback in a changing climate.

2 Methods

2.1 Study site

We configure our model to represent a field site in the Endalen valley on Svalbard (78°11' N, 15°44' E), about 5 km east of the main settlement of Longyearbyen. Thereby, we represent a realistic setup in terms of topography and weather conditions in a continuous permafrost landscape where observations are overall sparse, especially observations of groundwater flow. Our setup represents a sub-catchment on the north-west facing slope of the Endalen valley extending from the catchment border

located at the border between the slope and the adjacent plateau, and a groundwater spring located close to the main river of the valley (Fig. 2).

The catchment has been surveyed by drone in summer 2022 to produce a high resolution digital elevation model (5 × 5 cm; Schytt Mannerfelt, 2023, Appendix F). We delineate the photogrammetry-derived DEM using the catchment delineation procedure in QGIS (version 3.22.4). The landscape in the sub-catchment defined by a groundwater spring as discharge point is characterized by gentle slopes towards the valley bottom ($\sim 12°$) with gravely soils covered by a shallow organic layer, and a steep slope ascending towards the plateau ($\sim 37°$) characterized by a mostly gravely and rocky subsurface. Soil profiles in the surrounding areas have shown that a large part of the SOC is stored within near-surface layers in the TOL but that solifluction and cryoturbation have led to an increase in SOC also in deeper layers of sites in which cryoturbation processes are active (Weiss et al., 2017). However, this is only true for soil profiles close to the lower, gentle part of the slopes where at least a thin organic layer exists (Appendix B). The total catchment area is approximately $0.25\,\text{km}^2$, and the elevation difference between the groundwater spring and the uppermost edge of the catchment boundary is $376\,\text{m}$. For more, qualitative field observations please see Appendix B.

2.2 Model

To investigate coupled freeze-thaw dynamics with non-reactive transport, we use a physics-based cryohydrogeological numerical model, the Advanced Terrestrial Simulator (ATS v1.4.1, Coon et al., 2019). In its permafrost configuration, ATS couples the intricate interplay of freeze-thaw dynamics and both surface and subsurface energy, and hydrology (Painter et al., 2016) and has been successfully evaluated against multiple types of field observations (Jan et al., 2020; Painter et al., 2023). ATS employs an adaptive time-stepping scheme with user-defined minimum and maximum time steps. In this study, we set the minimum time step to 1e-10 days and the maximum to 1 day, allowing for efficient and accurate simulations across different seasons, which require higher or lower resolution time stepping, as well as for a user defined output interval. Solute transport in ATS is represented through the advection-dispersion equation,

$$\frac{\partial(\phi s_l C)}{\partial t} = -\nabla \cdot (qC) + \nabla \cdot (\phi s_l D_l \nabla C) + Q_s, \tag{1}$$

where ϕ is soil porosity (-), s_l is liquid saturation (-), C is solute concentration in the aqueous phase (mol solute mol water^{-1}), t is time, q is the Darcy flux vector (mol m^{-2} s-1), D is the hydrodynamic dispersion coefficient, and Q_s is a solute source/sink term (mol m^{-3} s^{-1}) (Molins et al., 2022). Note that solute is excluded from the ice phase by the formulation which represents solute as moles of solute per moles of liquid water and by the nonlinear solver which enforces solute mass conservation. Thus freezing of pore water results in an increase of solute concentration and the opposite is true for melting of pore ice. In the simulations performed in this study, dispersion is intentionally omitted by setting $D_l = 0$, focusing exclusively on solutes advected by water flow. This approach allows for the identification and analysis of the transient and seasonally variable flow field exhibited in the active layer, as well as the effects of freeze-thaw, cryosuction, wetting-drying in partially saturated soil, and unfrozen water seepage in permafrost. Although it would be valuable to consider dispersion, it is highly substrate-dependent
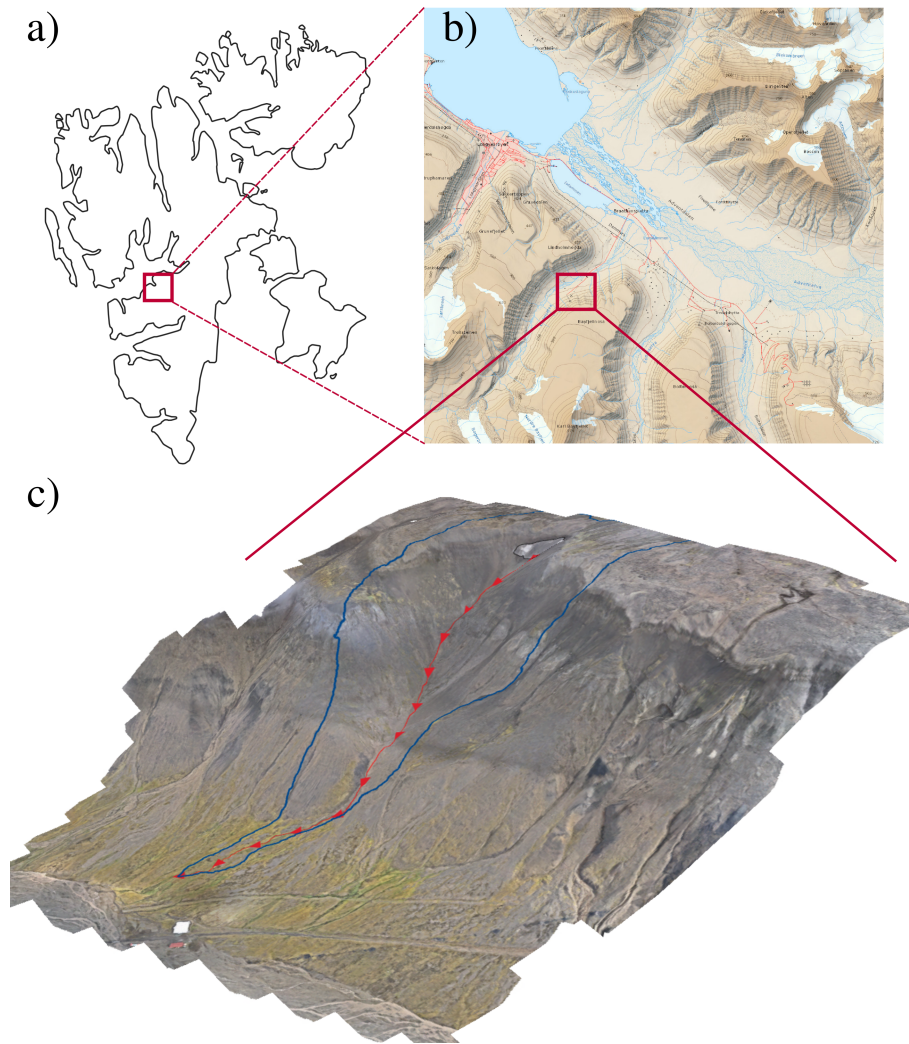
Figure 2. Overview over the study area. **(a)** Location of the study area within the Svalbard archipelago with the red box indicating the location of the Adventdalen valley close to the settlement of Longyearbyen. **(b)** Overview over the Adventdalen area with the red box higlighting the location of Endalen and the sub-catchment in question (map data based on Toposvalbard (Norwegian Polar Institue)). **(c)** 3D representation of the sub-catchment in Endalen, forming the basis for the model setup. The blue line outlines the catchment delineated based on the high resolution digital elevation model with QGIS. The red line with arrows indicates the path of highest flow accumulation within the catchment.

and challenging to quantify with field observations. Consequently, assuming dispersion coefficients would increase parameterization uncertainty and potentially obfuscate the advection-specific transport patterns caused by small-scale water movement such as percolation of unfrozen water at sub-zero temperatures or transport through capillary forces (such as cryosuction). Thus, the omission of dispersion ensures a clearer focus on lateral transport driven by advection, simplifying interpretation of
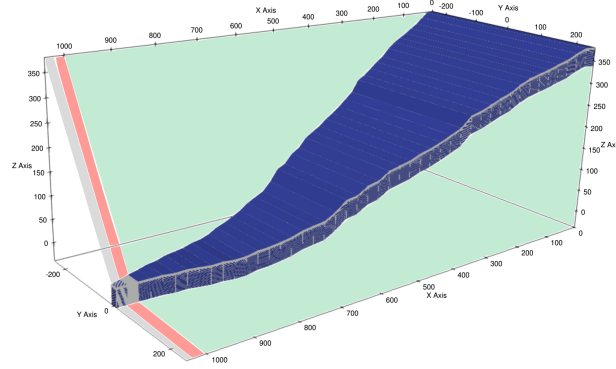
Figure 3. Representation of the mesh (blue shape) used for model simulations based on the catchment illustrated in Fig. 2. Dimensions of mesh elements vary in x-, y- as well as in the z-direction. The mesh (blue shape) represents a converging hillslope system with a wider width at the catchment boundary and a small width at the outlet. The green shaded area indicates the upper slope in which runoff is generated, the red area highlights the main area of interest later used in the presentation of the results, and the grey shaded area indicates the buffer zone. While the width (y-direction) increases uniformly with distance in the x-direction, column length in the x-direction is large in the upper part of the catchment ($\sim$23 m) and smaller in the last 40 m of the catchment (0.5 m between 1000 and 1020 m and 1 m between 1020 m and 1040 m). In the z-direction, cell resolution is higher (2 cm cell^{-1}) in the active layer (upper 1.2 m) and lower in the permafrost (up to 2 m cell^{-1}). The total depth of the domain is 40 m and the elevation is defined relative to the surface at the valley bottom, which is set to 0 m elevation.

the model's results. For a full description of the governing equations used in the permafrost configuration of ATS, please refer to Painter et al. (2016) and Atchley et al. (2015).

2.3 Mesh and boundary conditions

140 In this study, we employed a pseudo-3D variable-width mesh to capture the hydrological and thermal processes of the Endalen sub-catchment. The mesh extends 1040 m in the direction of highest flow accumulation and is of variable width in the direction perpendicular to flow to enforce the correct contributing area to each mesh cell on the surface. Such variable-width hillslope meshes preserve flow convergence, ensuring hydrological processes are well represented without the expense of a fully three-dimensional model (e.g., Fan and Bras, 1998; Troch et al., 2003; Hazenberg et al., 2015). In the direction of flow, the mesh is
145 divided into three key sections (see Fig. 3):

1. The upper slope (0-1000 m) – primarily serves as a water source (green-shaded area).

2. The main area near the valley bottom (1000-1020 m) – where transport experiments and tracer observations are conducted (red-shaded area).

3. The buffer zone (1020-1040 m) – designed to prevent boundary effects from influencing the simulation results (grey-
150 shaded area).

The mesh (blue body in Fig. 3) is coarser in the upper slope and refined in the lower areas to better capture fine-scale processes close to the valley bottom. This strategy, together with variable-width elements that preserve flow convergence, provides an accurate representation of catchment-scale processes without the computational burden of a full 3D model (Appendix A and D).

Boundary conditions are prescribed as zero-flux on the vertical side and the bottom. At the bottom (40 m depth), a constant temperature boundary condition of -6.6°C is applied, following borehole observations (Christiansen et al., 2020). At the surface, a surface energy balance, derived from average weather conditions in Adventdalen, governs energy and water exchanges between the surface and the atmosphere.

Soil physical properties are based on qualitative field observations and are defined to resemble highly conductive material (Table 1, Appendix B). A more detailed description of the mesh setup, boundary conditions, and soil physical properties can be found in the Appendix (Appendix A).

Table 1. Physical soil properties used in all model runs for the entire model domain.

Parameter	Unit	Value
Porosity	-	0.5
Permeability	m^2	2×10^{-11}
van Genuchten alpha α	Pa^{-1}	3×10^{-4}
van Genuchten alpha n	-	2
Thermal conductivity (saturated, unfrozen)	$W\,m^{-1}\,K^{-1}$	1
Thermal conductivity (dry)	$W\,m^{-1}\,K^{-1}$	0.29

2.4 Model spinup and initial conditions

To initialize the model, a 3-step spinup procedure is required (e.g., Jafarov et al., 2018; Jan et al., 2020; Hamm and Frampton, 2021). First, a single column model extending to the full depth of the final 2D mesh is used to establish an ice-saturated subsurface with an ice table near the surface. This was accomplished by freezing an initially hydrostatic and isothermal water column from below keeping an open top boundary to allow the volume expansion of the phase change to push out excess water. This sets a temperature of -6.6 °C at the bottom of the column and a permafrost table close to the surface. Second, the column model is run with the full forcing dataset until a cyclic steady-state is reached and year-to-year differences in e.g., daily ground temperature or evaporative flux are negligible. In the third step, the resulting column data is mapped to each of the columns in the transect, and the entire model is run again for ten years of average weather conditions accounting for all lateral processes such as lateral water flow and energy transport. We confirmed that the temperature is in a cyclic steady state at the end of the 10 year spinup period (Fig. D2).

The resulting subsurface state presents the initial conditions for the transient simulations. In total, there are five different transient simulation scenarios. The first one represents present-day weather and active layer development conditions. Two simulations represent gradual climate warming scenarios and two further simulations that mimic an abrupt increase in active layer depth (see Sect. 2.5 for in-depth descriptions of the scenarios). We consider a total of four tracer injection points in the

subsurface domain of the model: two tracers within the extent of the active layer and two within the upper permafrost (for exact locations see Fig A1). In the active layer, we define a tracer injection point representing TOL carbon consisting of recently deposited SOC close to the surface, and cryoturbated or buried carbon that has been vertically moved towards the bottom of the active layer and upper permafrost layers. Buried carbon can especially be found in solifluction-affected hillslope system, such as Endalen (see Fig. E1 and Weiss et al., 2017). The TOL carbon is injected close to the surface (0–2 cm below the surface) and the buried carbon is injected close to the bottom of the active layer (90–92 cm below the surface) in the first mesh column of the main area of interest of the mesh (x = 1000–1000.5 m, see Fig. A1). Both tracers are injected during fully frozen conditions from May 16 to 17 (24 hours). This ensures that they stay frozen and in place before the onset of thaw. The injection rate is a constant rate of $0.0012 \, mol \, s^{-1}$. This yields a total of 100 mol in the model, which is an arbitrary number to represent 100 units of solute. Since transport is conservative and non-reactive, the total mass of solute in the model will not change. The maximum simulated thaw depth (max. depth where the ground temperature $> 0 \, °C$) in the present-day model runs extends to 1 m.

Additionally, we define two injection points for tracers within the permafrost (representing ancient carbon): one close to the present-day active layer thickness (ALT; at 1.15 m depth) and one slightly deeper, just below the current permafrost table (at 1.55 m depth, see Fig. A1). These tracers are injected in the same mesh column, so that they have the same x-distance to the groundwater spring, and at the same time and rate as the active layer carbon tracers, yielding a total of 100 moles each.

2.5 Model forcing

The model forcing datasets for the different model scenarios represent different climatic conditions, depicting current conditions as well as gradually warming air temperatures, and two scenarios representing an abrupt deepening of the active layer.

Present-day weather conditions

To simulate active layer carbon transport, we use present-day weather conditions to run the model (the same forcing data as used during the spinup). This simulation is run for two years. We analyze transport times by observing the tracer breakthrough curve (BTC) at multiple distances relative to the injection point (at 10 and 20 m distance). In the model output, a BTC is defined when the concentration reaches a minimum threshold of 0.01 mol at a given observation point. We distinguish between surface and subsurface BTCs, with arrival times marked by the concentration exceeding and subsequently falling below this threshold. For surface transport of the buried tracer, however, the threshold is set to 0.0005 mol due to the small amount of mass transported along the surface. The thawing-out and mobilization of permafrost carbon is simulated in a different set of experiments described below.

Gradual warming scenarios

We simulate gradual permafrost carbon mobilization by incrementally increasing near-surface air temperature over a period of 50 years based on local predictions of air temperature trends in Svalbard (Hanssen-Bauer et al., 2018). The reference temperature is based on the current day-of-year average air temperature (T_{avg}), which is the only variable that changes over

time in the respective scenarios. We increase air temperature by applying warming rates specific for Svalbard of $0.125\,°C\,year^{-1}$ to represent an RCP8.5 scenario and a warming rate of $0.075\,°C\,year^{-1}$ for an RCP4.5 scenario (Hanssen-Bauer et al., 2018).

210 These warming rates are based on the predictions for air temperature increases by the end of the 21st century and are applied to each day of the year equally (season-specific warming trends are not considered here). This scenario is stylized and only aims to capture the effects of air temperature warming without considering complex, difficult-to-predict, and highly uncertain changes in precipitation. As we do not change the bottom boundary condition in these simulations, we confirmed with 1D simulations (Fig. D3) that the treatment of the lower boundary has negligible effect on the near-surface region of interest up to year 40 and

215 then only minor effects from year 40-50. Note that the mesh resolution in the upper slope area has been reduced by a factor of four (equivalent to halving the resolution twice, resulting in 23 m per column) to decrease the computational cost for these long-term scenarios. We have tested and confirmed that this reduction in spatial resolution does not significantly impact seasonal transport patterns, and we therefore do not anticipate long-term effects from the coarser mesh resolution (see Appendix D). Additionally, the output frequency has been reduced to monthly intervals to accommodate the extended simulation time and

220 manage data output over this period.

Abrupt active layer deepening

In two additional scenarios, we simulate abrupt active layer deepening by creating two scenarios with a single exceptionally warm year ($T_{avg} + 3\,°C$ and $T_{avg} + 5\,°C$, respectively). The warming is applied to each day equally. The purpose of this scenario is to create abrupt thaw of permafrost within a single summer, which represents and hyperbolizes the high interannual variation

225 in ALT observed in Svalbard (Strand et al., 2020). The abrupt deepening simulations are run for five years; two years of average present-day conditions to assure equilibrium conditions, one year of increased air temperature, and two more years of present-day conditions. The tracer in these simulations is injected in the first winter before the onset of the first thaw.

2.6 Potential mineralization rates

To further evaluate the importance of solute transport in the permafrost carbon cycle, we compute the potential for carbon

230 mineralization to CO_2 in the active layer throughout the thawing season based on the local prevailing environmental conditions in the soil in the present day scenarios. In this study, we do not consider mineralization into methane (CH_4), as the study site is located on a hillslope with rapid groundwater flow. Therefore, the production of methane is expected to be insignificant compared to those generated by wetlands (Denman et al., 2007). We calculate potential DOC mineralization depending on soil temperature following a Q_{10} formulation, and soil moisture following a threshold behavior function with an optimum liquid

235 saturation of 0.7 (Wen et al., 2020; Rawlins et al., 2021). While this formulation usually only accounts for a binary distinction between air and liquid saturation, we extended it by accounting for the presence of pore ice. For that, we multiply the function for liquid saturation by a function for air saturation, representing a threshold behavior with a maximum at 0.3 air saturation. Together, they represent soil moisture. Furthermore, since we do not work with absolute molar mass in this study, our potential for DOC mineralization solely depends on soil temperature and moisture (no kinetic rate constants or sorption parameters are

240 considered). Hence, the three-phase adjusted equation adapted from Rawlins et al. (2021) to derive mineralization rates in our model scenarios is

$$r_m = k_{decomp} f(T) f(S_l) f(S_a),\tag{2}$$

where r_m is the local potential mineralization rate (day^{-1}), k_{decomp} is the DOC mineralization rate coefficient as per Rawlins et al. (2021) (set to 0.83×10^{-2} day^{-1}) and $f(T)$, $f(S_l)$, and $f(S_a)$ are the temperature, moisture, and air saturation depen-

245 dencies, respectively. Functions for temperature dependence $f(T)$, moisture dependence $f(S_l)$, and air saturation dependence $f(S_a)$ are described using the Q$_{10}$ coefficient (Wen et al., 2020)

$$f(T) = Q_{10}^{|T-10|/10},\tag{3}$$

with T being local soil temperature and Q_{10} representing the mineralization rate increase per 10°C increase in temperature (in this case set to 1.7 according to Yurova et al. (2008) and Dusek et al. (2019)) and the threshold behavior functions (Wen

250 et al., 2020) for soil liquid saturation S_l and air saturation S_a described as

$$f(S_l) = \begin{cases} (\dfrac{S_l}{0.7})^{1.5}, & S_l \leq 0.7 \\ (\dfrac{1-S_l}{1-0.7})^{1.5}, & S_l > 0.7 \end{cases}.\tag{4}$$

$$f(S_a) = \begin{cases} (\dfrac{S_a}{0.3})^{1.5}, & S_a \leq 0.3 \\ (\dfrac{1-S_a}{1-0.3})^{1.5}, & S_a > 0.3 \end{cases}.\tag{5}$$

A plot showing the scaling effect of soil temperature and moisture for a range of -20–30°C for temperature and 0–1 for both liquid and air saturation is given in Fig. 4. The resulting mineralization rates are representative of a mineralization rate per day

255 and is highly dependent on soil moisture. In this formulation, mineralization results in 0 at fully saturated (S_l = 1 and S_a = 0) soil conditions due to oxygen deprivation. We chose this threshold behavior for soil moisture, because a linear behavior would result in most favorable conditions for mineralization under fully saturated conditions, which is not to be expected at the site.

Soil moisture and temperature conditions are extracted as a post-processing step within the present-day scenarios and do not affect the solute mass computed during the model run. Due to the large (monthly) output time-step size in the warming

260 scenarios, we did not calculate mineralization for these scenarios. Further, because the tracer used in this model does not chemically resemble DOC, carbon mass is not included in this formulation, and actual mineralization rates cannot be obtained. However, this approximation allows for a first order estimate of the fate of the modeled DOC upon release accounting for the hydrothermal dynamics in the active layer. Lastly, this formulation does not account for the possibility of methane production as it is not expected to be the dominant mineralization mode at the hillslope site in Endalen.
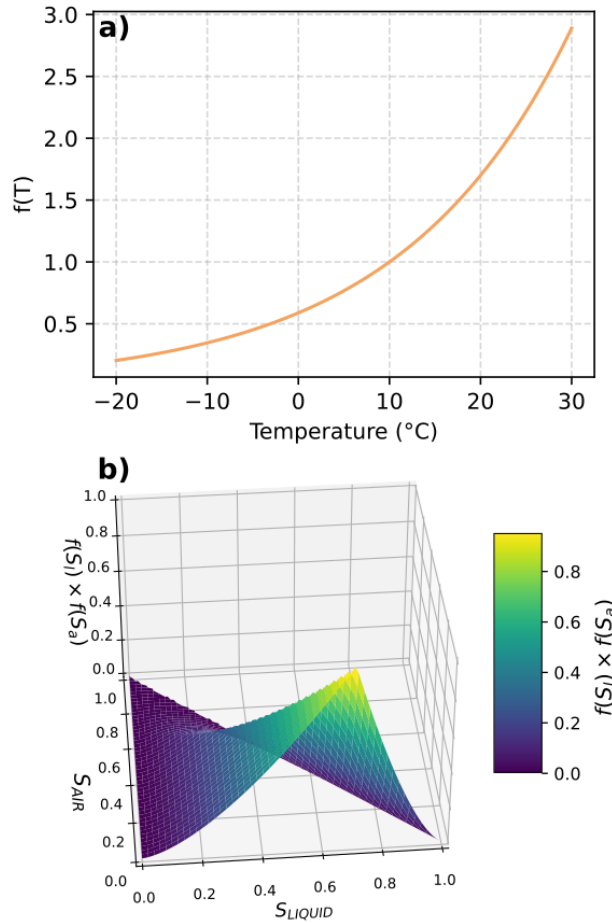
Figure 4. Functions **(a)** f(T) and **(b)** f(S_l) and f(S_a) using Eq. (3), (4), and (5), respectively, for a temperature range of -20–30°C and a liquid and air saturation range of 0–1. The value on the y-axis in **(a)** and z-axis in **(b)** corresponds to the scaling factor that is then used in Eq. 2.

3   Results

We evaluate solute transport by analyzing BTCs and tabulating peak as well as first and last arrival times of active layer carbon and ancient carbon, and by visualizing two-dimensional plume transport for each injected tracer. BTCs are obtained by vertically integrating a surface-subsurface column at 10 m and 20 m relative distance to the injection point for each given time step (for active layer carbon: minutes, for ancient carbon: days). The initial arrival and end of each BTC is defined by setting a threshold value of 0.01 mol. The arrival time is defined as the first day when the concentration exceeds 0.01 mol; the falling limb of the breakthrough curve is defined as the first day after the arrival time when the concentration falls below this threshold. The resulting value is a temporal snapshot of tracer mass at the given time. Hence, the BTC represents the temporal evolution of tracer concentration at a given location, showing how the concentration changes over time, though discretized due

to time steps in the model. The plume distribution, on the other hand, represents the spatial distribution of tracer concentration
at specific moments in time, showing how the tracer is distributed in space at a particular point in time. Arrival times are
expressed as dates within a year that represent present-day weather conditions in the study site.

3.1 Active layer carbon

Tracers injected at different depths in the active layer exhibit different breakthrough behaviors (Fig. 5). Most noticeable, tracer
breakthrough for both active layer sources occurs at different times throughout the warm season (June to October). Initial
mobilization of TOL carbon starts on 3 June during early active layer development and gets released from the initial point of
injection quickly (Fig. 6a and Table 2). During the early warm season, the active layer is shallow (thaw depth <10 cm) but
snowmelt infiltration as well as rain infiltration cause the thawed soil to be highly water saturated until mid-June. This leads to
ponded water on the surface from a horizontal distance of 1011 m onward allowing for rapid surface runoff and transport (see
Fig. 8). Surface transport is therefore responsible for 100% of the tracer mass passing through both observation points in the
early thaw-season and only lasts for 1 day at both observation points (Fig. 5a and b and Table 2). From mid-June onward, most
of the surface ponded water at the 20 m observation point infiltrates, reducing surface transport to essentially 0%. This aligns
with field observations, where snowmelt in early June led to fully inundated conditions across portions of the sub-catchment
surface, followed by drying as thaw depth increased and melt water can infiltrate into the subsurface (see Appendix B).

Table 2. Initial mobilization, first, last, and peak arrival of both active layer carbon tracers, including breakthrough times for tracer transported
in the subsurface and the surface. Note that a threshold value of 0.01 mol was applied to determine onset and end of the breakthrough curve.
This threshold value was set to 0.0005 mol for the buried tracer transported in the surface due to the small values. The arrival times are not
directly comparable to the above arrival times and are hence written in italics.

carbon source	initial mobilization	first arrival		peak arrival		last arrival		breakthrough time	
		10 m	20 m	10 m	20 m	10 m	20 m	10 m	20 m
TOL subsurface	3 Jun	4 Jun	5 Jun	6 Jun	7 Jun	10 Jul	28 Jul	35 days	53 days
TOL surface	3 Jun	4 Jun	4 Jun	4 Jun	4 Jun	5 Jun	5 Jun	1 day	1 day
buried subsurface	15 Aug	17 Aug	18 Aug	25 Aug	26 Aug	30 Aug	5 Sep	12 days	17 days
buried surface	*15 Aug*	*18 Aug*	*18 Aug*	*21 Aug*	*24 Aug*	*25 Aug*	*29 Aug*	*6 days*	*10 days*

The remaining tracer mass that has not been transported by surface runoff is transported with groundwater flow or seepage,
which starts at both observation points after mid-June, when all runoff is occurring in the subsurface. At the 10 m observation
point (Fig. 5c) peak arrival of the subsurface pulse can be detected on 6 June. With active layer deepening throughout the
warm season, the near surface layers become progressively less saturated as groundwater is restricted to deeper layers in the
subsurface. This leads to unsaturated flow and transport in the vicinity of the TOL tracer, slowly moving the tracer from the
10 m to the 20 m observation point. An initial subsurface pulse peak at 20 m can be seen just after the shift from surface- to
subsurface dominated transport on 7 June and can be attributed to the early active layer development, where the shallow active
layer is saturated. Most of the transport during this time happens at the surface, but as soon as surface water starts infiltrating
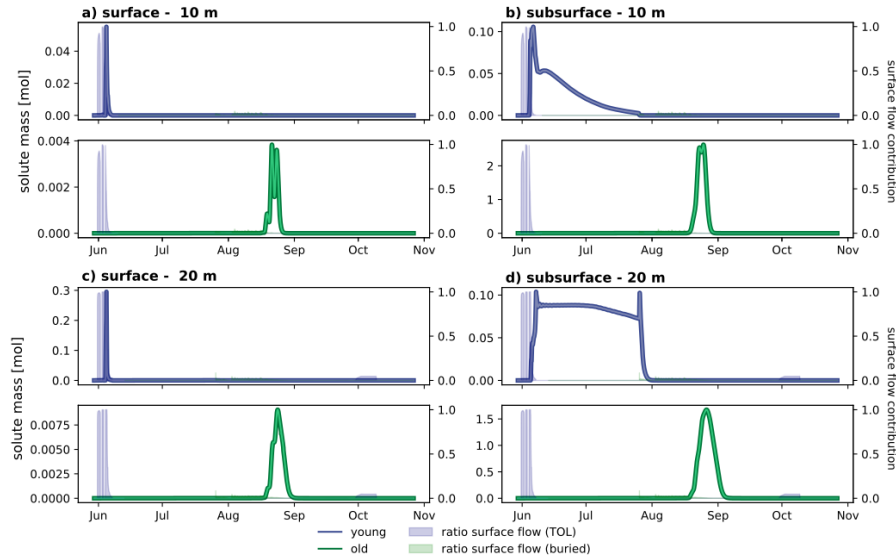
Figure 5. Tracer breakthrough curves (BTC) for **top organic layer (TOL)** carbon (blue line) and **buried** (green line) carbon tracer mass transported in surface runoff observed at (**a**) 10 and (**b**) 20 m relative distance to the injection point, and the tracer mass transported in the subsurface flow at (**c**) 10 and (**d**) 20 m distance. The blue and green shaded areas indicate the ratio (0–1) of transport on the surface as compared to the subsurface (0 = subsurface transport only, 1 = surface transport only). Note that the left y-axis scale varies between the four subplots to better visualize small amounts of transported mass.

in mid-June, it creates the first subsurface BTC peak. A second peak at the 20 m observation point on 26 July indicates the arrival of the remaining mass mobilized in the warm season. The abrupt end of the BTC can be attributed to the increasing liquid saturation in the end of July that enables rapid transport at fully saturated conditions. All in all, the BTCs suggest long
300   travel times in the subsurface upon initial release. The full range of breakthrough times from first arrival at 10 m (4 June) to last arrival at 20 m (28 Jul) amounts to a total of 54 days. Although the initial breakthrough is rapid and dominated by surface transport, the tail of the BTC is prolonged due to the residual mass experiencing unsaturated subsurface transport.

With a substantial amount of TOL carbon tracer mass transported during fully saturated conditions in the early active layer development, potential microbial mineralization rates are simultaneously low or even entirely absent (Fig. 7a). With
305   an increasing and drying active layer in late June and throughout July, mineralization rates are increasing close to the surface to a maximum of 2.9×10^{-5} day^{-1}. However, due to the transport behavior of the solute in the model, the tracer is mostly located in the highly saturated zone, where mineralization is very low or absent (e.g., on 14 June, Fig. 7a). This suggests that the majority of carbon in the TOL may experience transport before mineralization becomes significant enough to degrade it. Later in the season, when TOL carbon transport is slowed down due to unsaturated conditions in the topsoil, mineralization
310   will likely have an effect on the remaining solute mass and reduce the amount of potentially exported DOC.
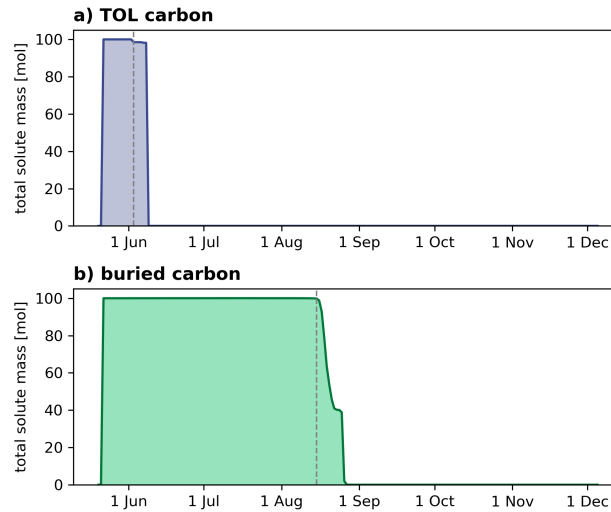
Figure 6. Mass release at the injection point of top organic layer (TOL) (a) and buried (b) carbon over time. Grey dashed lines indicate the timing of initial mobilization, which occurs when the thaw front reaches the solute injection depth (tracer mass < 99.9 mol, 3 June and 15 August for TOL and buried, respectively).

Buried active layer carbon mobilization only starts on 15 August, when thaw depth development has progressed and almost reached its maximum extent (Fig. 6b and Table 2). Due to its location close to the base of the maximum active layer thickness, the dominant mode of transport is almost exclusively through subsurface flow. Initial arrival at the 10 m and 20 m observation point is observed on 17 August and 18 August, respectively. The full range of breakthrough times compared to the TOL carbon transport is significantly faster (12 and 17 days at the 10 m and 20 m point, respectively, Fig. 5c and d; Table 2). Liquid saturation at the bottom of the active layer is high throughout the year, leading to saturated and therefore faster subsurface transport compared to unsaturated conditions.

A small fraction of buried carbon tracer (tracer mass < 0.005 mol) experiences surface transport (also visible in Fig. 9) because it gets transported upwards by groundwater upwelling. This is caused by a combination of the terrain unevenness and the undulating impermeable permafrost table, causing local downslope water accumulation and a fully saturated active layer. Arrival and breakthrough times for buried carbon transported in surface runoff in Table 2 are therefore based on a separate threshold value of 0.0005 mol. The fully saturated conditions throughout the active layer further lead to an absence of mineralization during most of the transport period in the model setup presented here (e.g., on 25 Aug, Fig. 7b).

In summary, the timing of initial mobilization due to the depth of each of the carbon pool tracers, and liquid saturation in the soil greatly determines the shape of the BTC and its potential for mineralization for each of the active layer carbon tracers. Unsaturated subsurface conditions lead to a prolonged tail in subsurface TOL tracer breakthrough and non-zero mineralization rates, while saturated conditions lead to a rapid, mostly symmetrical breakthrough of the buried carbon tracer and no potential for mineralization.
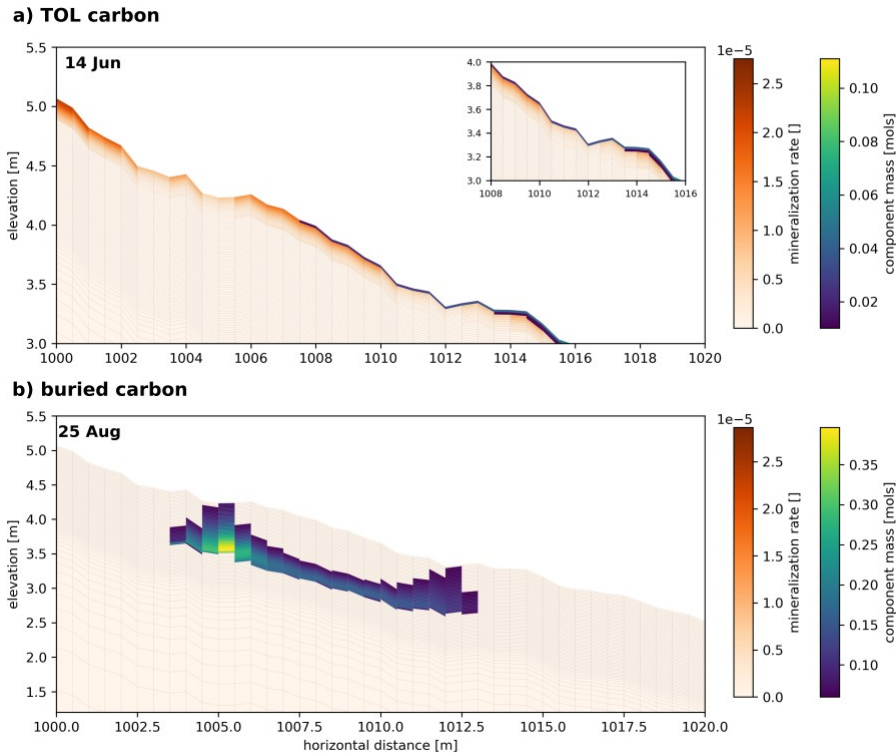
Figure 7. Temporal snapshot of potential normalized mineralization rate and component mass plume of (**a**) TOL carbon and (**b**) buried carbon spreading throughout the transect on 14 Jun and 25 Aug, respectively. Light-orange areas mark comparably low potential mineralization rates, dark-orange areas indicate the highest potential for mineralization. Component mass for the selected date (14 Jun and 25 Aug) is added as a blue to yellow overlay. Note that the tracer mass is restricted to the uppermost subsurface cell and masked to only represent values > 0.01 mol (for TOL carbon) and 0.06 mol (for buried carbon). The inset at the top right in panel (**a**) shows a zoomed-in version of the area in which tracer is present.

The spatial distribution and spreading of the tracers within the transect are analyzed by visualizing temporal snapshots of the plume in 2D subsurface cross plots. Solute movement of the TOL carbon tracer is strongly limited to the surface and the uppermost soil layers (up to 10 cm below the surface) and does not significantly spread into deeper soil layers even after deeper active layer development (Fig. 8). Note that in this figure, only subsurface mass transport can be visualized. The subsurface plume spreads slowly and has not reached the 20 m observation point by the last temporal snapshot shown here (20 June). This highlights the significantly slower rate of unsaturated transport as compared to saturated transport, which is predominantly responsible for the rapid transport of buried carbon (Fig. 8). Here, the plume movement is largely uniform in the subsurface. Due to the unevenness of the terrain and highly saturated conditions, some tracer mass is transported upwards towards the surface (e.g., at 1005 m on 23, 25, and 27 August in Fig. 9), but the amount of buried carbon tracer being transported on surface is small (max. 8% on 26 July, Fig. 5b and d, green shaded area).
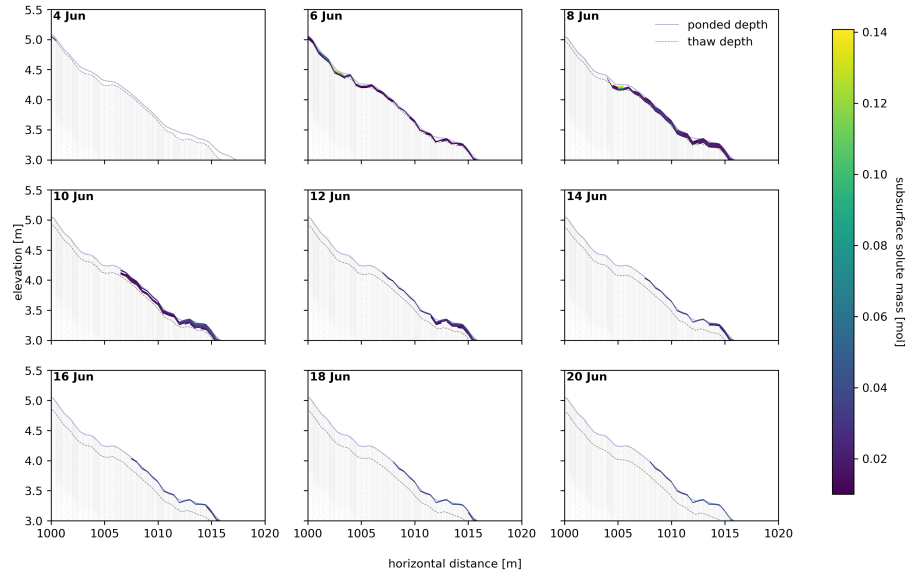
Figure 8. 2D representation of the top organic layer (TOL) carbon plume dispersion between the point of tracer injection (x = 1000 m) and the last observation point (x = 1020 m) for selected dates during summer after tracer injection. Elevation is given in relative elevation to the conceptual valley bottom (surface of the valley bottom = 0 m). Tracer mass is given in mol and is masked to only represent values > 0.01 mol. The blue solid line marks the water table above the surface (ponded depth), the black dashed lines indicates the thaw depth at each date.

3.2 Ancient carbon

Gradual warming scenario

Carbon mobilization as simulated in the gradual warming scenarios RCP4.5 and RCP8.5 exhibit distinctly different transport patterns from active layer carbon transport. Within the first year and in both gradual warming simulations, before air temperature warming has even affected the ALT, vertical mass movement of the upper ancient carbon tracer (ancient C at 1.15 m depth) can be observed. A substantial fraction of the initially injected tracer mass ($\sim$40%) moves vertically (both upwards and downwards) within the same mesh column in which it was injected (see Fig. 10a and d and Fig. 11). This way, carbon gets vertically distributed over the first four years, before the active layer has deepened sufficiently to allow for lateral transport to move tracer mass out of the initial column of injection. This observation can be attributed to percolation (during thaw) and cryosuction (during freeze-up). When the active layer is developing in the late thawing season, some tracer moves vertically downwards into partially frozen layers while the opposite occurs during the freeze-up when the freezing front from above draws water towards it due to capillary forces referred to as cryosuction.

From the fourth year onward, a small fraction (0.02–0.08 mol in the RCP4.5, Fig.10b and c, and 0.025–0.125 mol in RCP8.5, Fig.10e and f, respectively) of the ancient carbon source injected at 1.15 m depth arrives at the 10 and 20 m distance observation points. At the 10 m observation point, annually recurring breakthrough curves are lasting for a short amount of time (component
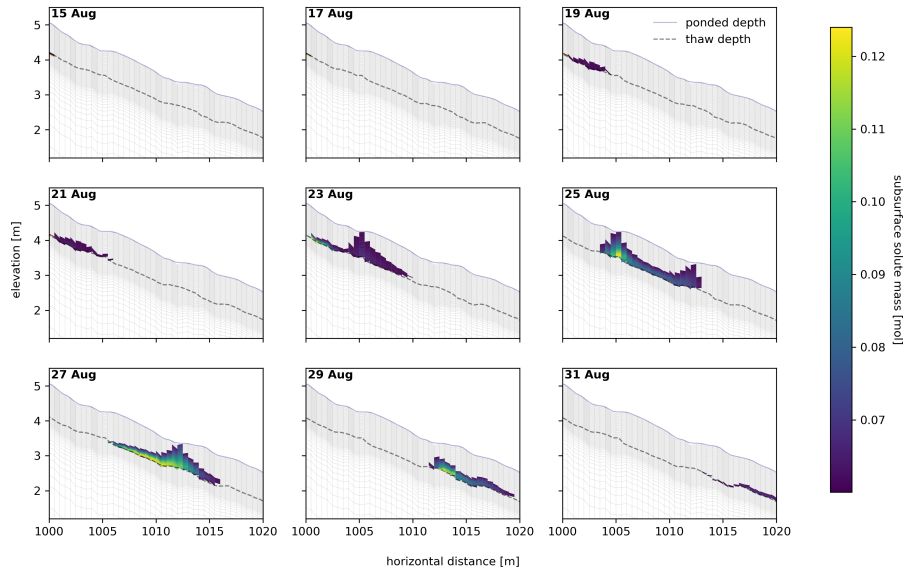
Figure 9. 2D representation of the buried carbon plume dispersion between the point of tracer injection (x = 1000 m) and the last observation point (x = 1020 m) for selected dates during summer after tracer injection. Elevation is given in relative elevation to the conceptual valley bottom (surface of the valley bottom = 0 m). Tracer mass is given in mol and values < 0.06 mol are masked for better visualization. The blue solid line marks the water table above the surface (ponded depth), the black dashed line indicates the thaw depth at each date.

mass > 0.01 mol from mid-September to mid-October) with all the mass that has been released from the source during the respective summer arriving at 10 m and leaving the observation point within this time.

At 20 m, first tracer arrival starts within the same time after the beginning of the simulation as at the 10 m observation point, but instead of being flushed through the observation column, this tracer accumulates within the observation column with short periods of release (less than 2 weeks) during the late autumn (mid September to mid October) and becomes immobilized upon freeze-up until it thaws out in the following season.

All mass (transported molar mass ≥ 95%) of the ancient carbon pool at 1.15 m has been laterally transported from the injection column after 34 years in the RCP8.5 scenario. In the RCP4.5 scenario, 50 years of gradual warming have led to a release of 93.5% of the ancient carbon tracer mass (Fig. 10a and d). Tracer arrival at the observation points is relatively even throughout this period indicating no abrupt release as a result of gradual warming.

A similar behavior can be observed for the ancient carbon pool at 1.55 m depth. Mobilization and lateral transport of this carbon pool (mass in injection column < 99%) starts after 33 years in the RCP8.5 scenario and after 48 years in the RCP4.5 scenario. By the end of the 50 year period, 85% of the mass in the injection column has been released in the RCP8.5 scenario. Towards the end of the simulation time, an abrupt release of the carbon pool tracer at 1.55 m can be seen. This is likely due to the formation of a talik beginning in the winter between years 48 and 49. The initial talik encompasses the ancient carbon injection cell at a depth of 1.15 m, allowing for extended transport periods, including during winter.
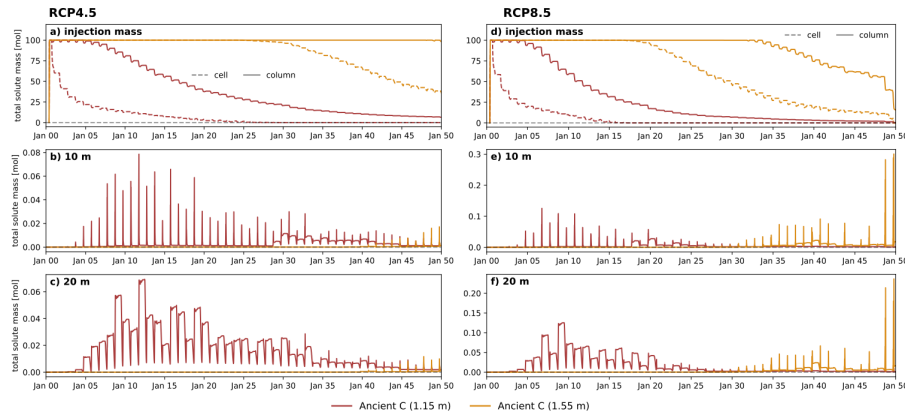
Figure 10. Ancient carbon mobilization upon gradual warming in the RCP4.5 (**a-d**) and RCP8.5 (**d-f**) scenario simulations. Tracer injection mass (**a** and **d**) indicate when the tracer gets mobilized at the initial injection point in the respective cell (dashed line) and integrated vertically over the entire injection column (solid line). Red and orange lines represent ancient carbon in 1.15 m and 1.55 m depth, respectively. When molar mass reaches 0, all tracer has been laterally transported away from the injection point. Tracer BTCs at 10 m (**b** and **e**) and 20 m (**c** and **f**) show the arrival times of tracer mass released at the injection column. Note that rounding errors of small amounts of mass have led to a tracer mass > 100 mol when integrated over the entire column. Hence, values > 100 mol were truncated to 100 mol. For details see Appendix C.

370   In the RCP4.5 scenario, only 1% of the tracer mass at 1.55 m depth has been released by the end of the simulation. Due to the post-processing procedure of the model output in which we integrate molar mass vertically throughout the injection column, rounding errors cause the total molar mass in the injection column to slightly exceed the initial mass of 100 mol (see Appendix C). This does not represent a physical increase in mass. It can therefore not conclusively be determined when exactly lateral movement of the tracer in 1.55 m depth was initiated. However, vertical mobilization of this tracer can be observed starting after

375   27 years, causing a vertical redistribution of 65% of the initially injected mass by the end of the simulation period. In summary, these results suggest that gradual warming leads to gradual release of ancient carbon pools with significant redistribution in the vertical directions.

Abrupt active layer deepening

In the case of the abrupt active layer deepening scenarios, tracer mobilization of ancient carbon is more similar to the behavior

380   of buried active layer carbon released by seasonal thaw (Section 3.1). In the year of abrupt active layer deepening, ALT reaches 1.35 m (+35 cm compared to present-day ALT) and 1.6 m (+60 cm compared to present-day ALT) in the +3 and +5 °C scenarios, respectively. Such variability is not unprecedented. Strand et al. (2020) showed that variations in active layer depth in Adventdalen between cold and warm years can reach up to 30 cm. Our simulations fall within this range, but intentionally amplify the effects of an exceptionally warm year on active layer dynamics, resulting in an exaggerated active layer deepening

385   by a factor of two. The abrupt deepening causes the entire BTC of the ancient carbon tracer at 1.15 m depth to start and finish
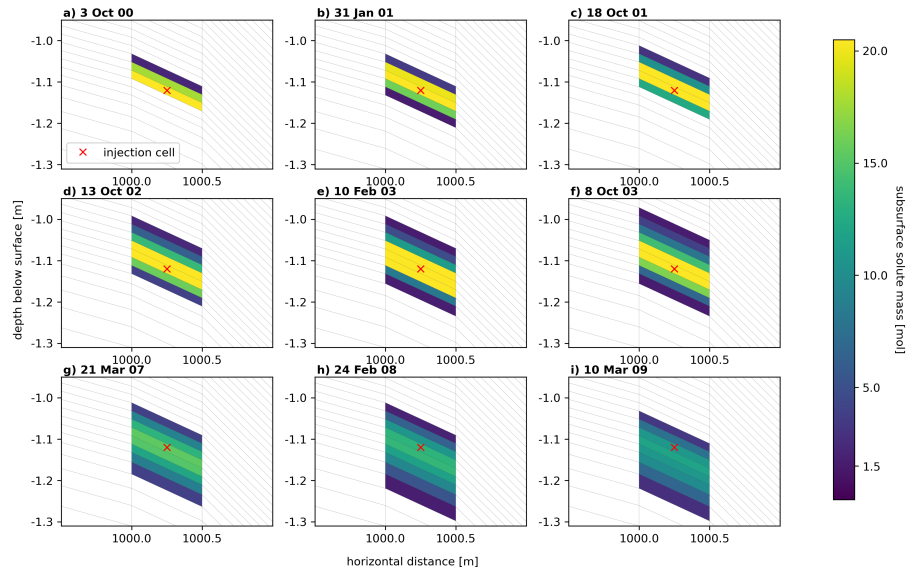
Figure 11. Representation of the vertical redistribution of tracer from the initial injection cell (red cross) throughout the depth profile of the injection column. (**a-c**) indicate the distribution throughout a full freeze-thaw cycle, (**d-f**) represent vertical redistribution from the third to the fourth freeze-up including the mid-winter vertical movement of the second freeze-up, and (**g-i**) represent vertical distribution by the end of the first modeled decade. Mass is depicted in molar mass and only values larger than 1.5 mol are shown, the remaining mass is masked for better visualization.
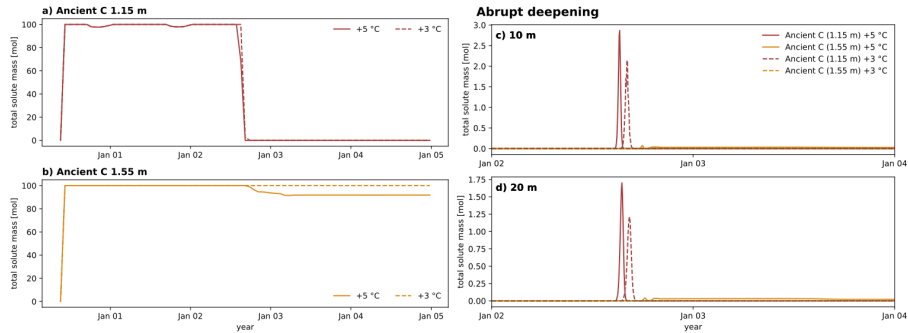
Figure 12. Mobilization of ancient carbon upon abrupt active layer deepening. The injected tracer mass (**a** and **b**) indicates when the tracer gets mobilized at the initial injection point in the respective vertically integrated injection column. Solid and dashed lines represent injection mass mobilization under the +5 °C and the +3 °C scenario, respectively. Tracer BTCs at 10 (**c**) and 20 m (**d**) indicate when and how fast the tracer passes through the observation column. Red and orange lines represent the tracer representing ancient carbon at 1.15 m and 1.55 m depth, respectively. Note that rounding errors of small amounts of mass have lead to a tracer mass $>$ 100 mol when integrated over the entire column. Hence, values $>$ 100 mol were truncated to 100 mol. For details see Appendix C.

within the same year and initiates the release of the tracer at 1.55 m in the +5 °C scenario (Fig. 12). Tracer molar mass of 0.05 mol (ancient C at 1.15 m depth) is exceeded on 13 August and falls below 0.05 mol on 27 August (duration: 14 days) at both the 10 and 20 m observation points in the +5 °C scenario. In the +3 °C scenario, these dates are 24 August and 14 September (duration: 21 days). For the ancient carbon tracer at 1.55 m depth, a small breakthrough of max 0.07 mol at the 10 m observation point and max 0.04 mol at the 20 m observation point can be observed in the +5 °C scenario. In the +3 °C scenario, this tracer remains frozen in the year of abrupt active layer deepening.

Observations of molar mass in the injection points in both simulations show that all mass of the ancient carbon at 1.15 m depth is released from the injection column within year two. In the +5 °C scenario, the ancient carbon at 1.55 m depth indicates partial lateral release of ∼ 8% of the injected mass by the end of year two. After full freeze-up in year three, the mass stays constant throughout the following two summers, indicating no further release of tracer after the isolated abrupt active layer deepening event.

4   Discussion

Through our model experiments, we identified different transport patterns for different carbon pool representations within the active layer and in the permafrost. We find that TOL carbon pools may experience fast initial transport during early active layer development, but also show prolonged residence times due to unsaturated conditions in the subsurface. Buried active layer carbon, on the other hand, moves fast upon release in the saturated part of the active layer (confirming hypothesis (i)). Slower transport indicates longer residence time in the unfrozen soil upon thaw, while fast transport decreases the residence time.

The transport patterns observed in the buried carbon tracer do not carry over to the ancient permafrost carbon that is initially frozen and only gets mobilized upon ALT increase through gradual air temperature warming (confounding hypothesis (ii)). Instead of being flushed out when exposed to groundwater flow, the tracers that represent ancient carbon experience gradual release at increasing rates with increasing permafrost degradation. With rising temperatures near the thaw front, a small fraction of unfrozen water gets mobilized at sub-zero soil temperatures, enabling minor vertically downward migration in the soil profile without experiencing significant lateral movement. During annual freeze-up, cryosuction (capillary forces causing water to be drawn to the freezing front) causes some fraction of the water and the tracer in it to be vertically migrated upward, moving it closer to the depth of maximum ALT. Here, it is more likely to get thawed out during the next summer, contributing to the small, but recurring, annual releases. Cryosuction has previously been observed to be of importance in a polygonal tundra model with analysis of solute transport (Jafarov et al., 2022), and our results here suggest the importance of cryosuction not only applies to predominantly flat terrain with microtopography, but also within hillslope systems where the thaw front progressively increases. This indicates the potential for cryosyction-induced dispersion of solutes, highlighting the importance of representing this process in climate warming scenarios. Note that explicit dispersivity was omitted in the model (see Section 2.2) and is therefore not responsible for this observation. We argue that, had dispersivity been included, this result might have been obscured, potentially leading to a misinterpretation of cryosuction's role in solute transport as substrate-dependent dispersion.

Under the assumption of an abrupt increase in ALT due to one very warm year (T_{avg} +3, +5), the transport of ancient, currently frozen carbon tracer becomes more similar to the transport of buried carbon. Due to the short-term but significant increase in ground temperatures, the entire injected tracer mass is mobilized as soon as the active layer thaw front reaches the depth of the carbon source. The rapid export of this carbon source suggests that the residence time is short leading to decreased potential for microbial mineralization.

A thought experiment in which we calculated potential microbial mineralization as part of the post-processing of environmental soil temperature and moisture shows that the high liquid saturation associated with rapid transport also leads to reduced or absent mineralization throughout most of the active layer. Under generally or future drier conditions (Painter et al., 2023), mineralization rates in the active layer may be higher, especially in the upper part, where fully saturated conditions appear mostly in the beginning of the season. Translating this result to the transport patterns in the gradual and abrupt warming scenarios, this may imply that permafrost carbon can experience export in the form of DOC before it gets a chance to be mineralized into CO_2. However, these results rely on a threshold assumption for the effect of soil moisture on mineralization (Wen et al., 2020), which is uncertain and requires increased attention in future research to better constrain microbial mineralization in permafrost affected landscapes.

The simulations conducted in this study are based on environmental and general soil physical conditions observed in the Endalen valley, Svalbard. However, the model is limited by the availability of observational data for e.g., soil properties and subsurface conditions such as preferential flow paths. Furthermore, it does not account for a full 3D representation of the area as there is no additional discretization in the transverse direction. We partly address this by representing a converging slope model setup, where the cell width in transverse direction varies depending on the distance in longitudinal direction. This way, the surface area of the catchment is preserved, and it is possible to accurately represent water and energy balances as well as infiltration and evaporation rates throughout the catchment. This approach has previously been applied by Gao and Coon (2022). The subsurface material used in our simulations represents a highly conductive soil that allows for fast groundwater seepage from up- to downhill. At the field site, this is a realistic assumption as the ground is dominated by gravely soil overlain by a thin organic layer, but may be different for hillslope systems with finer material such as silts and clays.

While the Endalen valley represents a single case within the context of high Arctic hillslope systems underlain by continuous permafrost, similar systems are widespread across the Arctic, making this site a valuable example for studying permafrost carbon transport. The slope of approximately 12° in our study area is representative of gently sloped terrain in permafrost landscapes, which accounts for about 20% of the total permafrost region, commonly found in areas such as Greenland and parts of Canada (Hamm and Frampton, 2021). However, our findings may not be directly transferable to other permafrost settings, such as flat terrain, where differences in groundwater flow velocities, saturation levels, and small-scale processes like cryosuction could significantly alter transport dynamics, especially in landscapes influenced by microtopography, such as polygonal tundra. Additional studies across a variety of terrains, supported by reliable field observations, are necessary to gain a more comprehensive understanding of lateral carbon transport in permafrost environments.

Enhancing our understanding about potential lateral export of carbon is crucial for reducing the uncertainty surrounding the permafrost carbon feedback and the fate of permafrost carbon (Intergovernmental Panel On Climate Change (IPCC),

2022). Advances in research on the permafrost carbon feedback have been made by simulating production, transport, and transformation of carbon in the contemporary carbon cycle across landscapes using land surface models (Bowring et al., 2019, 2020) or by characterizing fluvial derived organic carbon in rivers through radio carbon dating (Wild et al., 2019). However, a mechanistic representation of in-situ mobilization of permafrost carbon in models is generally lacking, and have only begun to be developed (Rawlins et al., 2021; Mohammed et al., 2022). In this study, we address this process by simulating the thaw out and mobilization of permafrost carbon with a 2D hillslope model, only accounting for non-reactive transport of a generic tracer. While our model gives us valuable insight into the mechanisms causing transport to be slower or faster, a full depiction of carbon is not included since representing carbon specifically would require extensive in-situ soil carbon characterization, and representation of biogeochemical reactions and processes such as microbial mineralization, which are currently not part of the model setup.

Increasing the terrestrial-to-aquatic transport of permafrost carbon can influence the further processing of such carbon and its effects on the oceans. Generally, at least half of the carbon input from terrestrial sources into the aquatic systems is expected to be released to the atmosphere within the riverine system (Cole et al., 2007). However, field sampling of dissolved organic matter (DOM) in Alaska has shown that the organic matter available for export may have low biolability (Mutschlecner et al., 2018). This suggests that the more stable ancient permafrost carbon may indeed experience export into rivers and the ocean without getting entirely mineralized beforehand.

While this study mostly focuses on the potential of carbon transport, the results can also provide valuable insights into contaminant transport, in order to evaluate the importance of hydrology in contaminated sites in permafrost regions and how contaminants may move within the subsurface. Contaminated sites with toxic substances are likely to impact livelihoods and ecosystems in the Arctic and require increased attention (Langer et al., 2023). The modeling approach presented here offers a basis for further development for both carbon transport as well as contaminant transport.

To address these problems more comprehensively, the use of a reactive transport model will help to disentangle the aforementioned complex interactions (e.g. Mohammed et al., 2022). For example, biogeochemical carbon dynamics can be incorporated into the model by assigning chemical properties to the tracer as well as describing microbial mineralization processes based on environmental variables such as soil moisture and temperature. However, the complexity of these processes alone adds significantly to the existing complexity of representing freeze-thaw dynamics in permafrost regions and poses a considerable computational challenge.

Permafrost carbon stock databases such as the one by Hugelius et al. (2014) can further be used to model site-specific conditions based on the presence of permafrost carbon in different depths. In the same way, chemical properties can be assigned to contaminant species. Integrating transport as well as biogeochemical reactions of the dissolved compounds in permafrost hydrological models will then help to further constrain global climate models and reduce the uncertainty surrounding the permafrost carbon feedback.

5   Conclusions

The fate of permafrost carbon in a changing climate is an essential part of the permafrost carbon feedback loop. Considerable uncertainty in predicting the effects of permafrost thaw evolve around the uncertainty in how much of the carbon currently immobilized in permafrost gets released vertically to the atmosphere as GHGs and which fraction of it might get transported laterally towards surface water and eventually to the ocean. In this study, we addressed the transport component of this question. For solute transport in the seasonal active layer, we find that:

1. A tracer representing active layer carbon experiences different transport velocities depending on its location within the active layer.

2. Active layer carbon close to the surface experiences both rapid surface transport but also prolonged subsurface transport due to unsaturated conditions close to the ground surface as the thaw front propagates deeper in the ground.

3. Active layer carbon close to the bottom of the active layer experiences faster subsurface transport and no surface transport due to saturated conditions at the depth of ALT.

4. Carbon released near the base of the active layer may experience limited mineralization prior to export due to the combination of relatively rapid transport with groundwater and limited microbial mineralization rates due to saturated conditions.

In a warming climate, solutes such as carbon released from the permafrost, are likely to experience different transport patterns. Our main findings for simulations of a warming climate are:

1. Under the simulated environmental and soil physical conditions in this study, a gradual warming of air temperature with climate change may lead to a gradual release of currently frozen carbon pools. While moving vertically downward over time, small amounts of carbon can get released laterally every year, but a rapid release of large amounts of carbon at once are not expected. This may favor the the in-situ mineralization of the carbon prior to export.

2. Abrupt active layer deepening, on the other hand, may lead to the rapid release and transport of SOC in the form of DOC, leaving little time for microbial mineralization when the soil is unfrozen.

3. Seasonal thaw and freeze-up enhances vertical movement of solutes by cryosuction, which can enable an earlier than expected onset of release near the permafrost table.

Code and data availability.   The Advanced Terrestrial Simulator (ATS) (https://doi.org/10.11578/DC.20190911.1; Coon et al., 2019) is open source under the BSD 3-clause license and is publicly available at https://github.com/amanzi/ats (last access: May 2023) (Coon et al., 2016). Simulations were conducted using version 1.4. Forcing datasets and input files are available at https://github.com/a-hamm/hamm-et-al-2024-permafrost-transport. Weather data to create the forcing dataset were downloaded from https:

515 //www.unis.no/resources/weather-stations/ (The University Centre in Svalbard, 2023) and from https://seklima.met.no/observations/ (Norwegian Climate Service Centre, 2023). The drone survey images for the sub-catchment in Endalen is available at https://doi.org/10.5281/zenodo.8279263 (Schytt Mannerfelt, 2023).

Appendix A: Mesh and Boundary Conditions

To capture the main topographical characteristics of the Endalen sub-catchment, a variable-width representative-hillslope mesh was created, extending 1040 m along the highest flow accumulation path from the catchment boundary (376 m relative elevation) to a groundwater spring at the valley bottom (0 m relative elevation). A critical consideration in the mesh design was ensuring that the full catchment area was represented. This is important because precipitation falls across the entire catchment and can run off into the main area of interest. If the entire catchment surface area were not accounted for, a significant portion of the water from precipitation would be missed, leading to unrealistic hydrological conditions. The mesh follows a pseudo-3D approach, where the width of mesh elements varies along the y-axis. This method allows for capturing essential hydrological and thermal processes across the catchment without the computational expense of a fully 3D model, preserving flow convergence, which is crucial for surface and subsurface flow dynamics. The plan shape and profile curvature of the catchment, dominant topographic controls on flow (Dunne and Black, 1970; Anderson and Burt, 1978), are preserved by the variable-width mesh.

The use of a variable-width representative-hillslope mesh is a well-established modeling approach in catchment and hillslope hydrology. The sides of the hillslope are determined from topography by gradient descent, aligning the sides with surface flow and allowing for no-flow boundary conditions on the sides. This approach has a long history in catchment hydrology (e.g. Fan and Bras, 1998; Troch et al., 2003; Hazenberg et al., 2015) and has been successfully compared to three-dimensional models (e.g. Paniconi et al., 2003; Hazenberg et al., 2015)

The mesh is divided into three sections:

1. **Upper Slope (0-1000 meters in the x-direction)**: The horizontal resolution of this area is 5.8 m (23 m for the climate change scenarios) along the x-direction and varies in width along the y-direction. This section acts as the main water source for the catchment. The coarse resolution in the upper slope helps reduce the computational costs for these process-rich simulations on a sub-catchment scale. Note that horizontal resolution in the upper slope area is reduced by a factor of four (23 m) for the climate change scenarios due to the high computational costs. The upper slope, due to its low SOC abundance (Weiss et al., 2017), is not considered for solute transport in this study.

2. **Main Area of Interest (1000-1020 meters)**: The horizontal resolution increases to 0.5 m to account for the more detailed hydrological processes occurring near the valley bottom, particularly solute transport. Closer to the valley bottom, where more SOC can be found (Weiss et al., 2017), and where the modeled tracer is injected (see Fig. A1) and breakthrough is observed, this finer resolution allows for more accurate modeling of transport processes.

3. **Buffer Zone (1020-1040 meters)**: The horizontal resolution is increased to 1 m in the x-direction in this area, which acts as a buffer zone where water can accumulate in the subsurface toward the end of the transect. The boundary condition prescribed at the surface of the last column allows water to leave the system at the surface of the last mesh column. To avoid misinterpreting these artifacts as hillslope processes, this zone is not central to the analysis of the results and is implemented based on methods established by Jan et al. (2020) and Hamm and Frampton (2021).
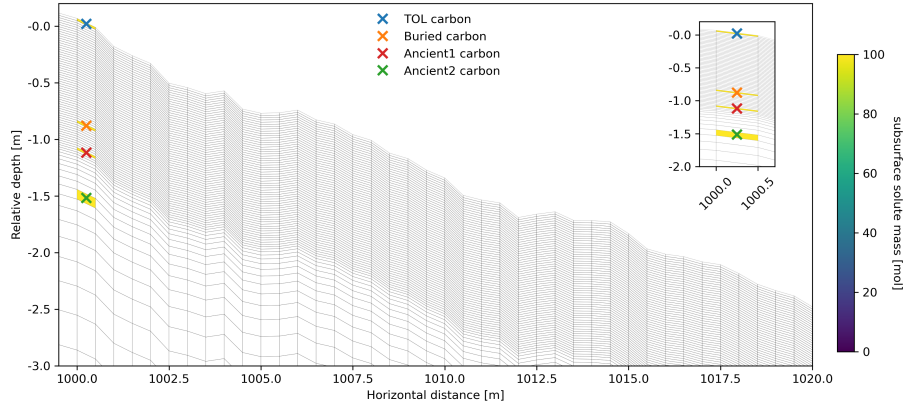
Figure A1. Visualization of the injection cell locations within the model domain.

In the y-direction, the mesh extends from 20 m at the lower end of the catchment to 500 m width at the upper catchment boundary. In the z-direction, the mesh follows the topographic profile based on the path of highest flow accumulation extracted from a high-resolution DEM. The vertical depth of the mesh is 40 m, discretized into cells with variable vertical resolution. Near the surface, the resolution is set to 2 cm to capture the dynamics of the active layer and freeze-thaw processes, while

555 deeper layers within the permafrost have a coarser resolution of up to 2 m. This layered vertical approach ensures accurate representation of the subsurface's thermal and hydrological behavior, critical for modeling seasonal variability in the active layer.

The mesh was generated using a Python script provided in the ATS repository. The slope of the triangular shape of the mesh resulting in the variable within y-direction is determined by the user-defined minimum width (20 m) and maximum width

560 (500 m) of the mesh. These measurements will define the outer edge of the lowermost and uppermost column, respectively. The slope for each column in between is then calculated using the following equation (Eq. A1):

$$slope = \frac{y_{head} - 0.00025}{x_{max} - x_{min}} \tag{A1}$$

Where y_{head} is the half the difference between minimum and maximum width (here: $(500 - 20)/2 = 240$) and x_{max} and x_{min} are the maximum and minimum value in x-direction. The actual width in y-direction for both edges of each column in

565 x-direction is then calculated by (Eq. A2):

$$y_0 = y_{\text{tail}} + slope \cdot (x - 40) \tag{A2}$$
$$y_1 = y_{\text{head}} - slope \cdot (x - 40) \tag{A3}$$

with y_0 being the upper edge and y_1 being the lower edge. y_{tail} is the negative of half the difference between minimum and maximum width (here: $(500-20)/-2 = -240$) and x is the distance in x-direction. The resulting mesh is symmetric, centered

570 around $y = 0$, and its surface area corresponds to the catchment area based on the DEM used to delineate the sub-catchment in Endalen.

Boundary conditions are prescribed for all external model surfaces. Vertical sides are assigned zero-flux boundaries for water and energy, restricting lateral flow to the surface at the downslope boundary. Surface runoff occurs once ponding exceeds the surface elevation. At the bottom boundary, a no-flow condition is imposed, with a constant temperature of -6.6°C, following

575 borehole observations (Christiansen et al., 2020). At the top boundary (surface), a surface energy balance, which serves as a source and sink for water and energy in the subsurface, is derived from site-specific weather data. Data from a nearby weather station in Adventdalen, approximately 3 km northeast of the study site, is used for air temperature, vapor pressure, incoming shortwave radiation, wind speed, and precipitation. Precipitation data is supplemented by the Longyearbyen airport weather station, 10 km northwest of the study site.

580 The forcing datasets contain daily values for all variables. Except for precipitation, a day-of-year average from the years 2013 to 2020 is used to describe a typical yearly cycle representative of present-day weather conditions. Precipitation is split into rain and snow based on air temperature (rain for T > 0°C, snow for T ≤ 0°C) and distributed throughout the year using a frequency-density function to match the statistical characteristics of observed rainfall (Magnússon et al., 2022). This method avoids distributing the total precipitation evenly over the respective rain and snowfall periods, which would result in small

585 daily precipitation rates that promote evaporation and limit infiltration, reducing soil moisture, and no days with absolute zero precipitation. The total sum of precipitation equals the average sum recorded between 2013 and 2020, with 84 mm of rain and 115 mm of snow. By using a frequency-density function, the resulting distribution more closely resembles natural rainfall variability, ensuring a realistic representation of precipitation events. This precipitation model plays a critical role in shaping the hydrological and thermal balance within the soil.

590 The soil physical properties were defined to resemble highly water-conductive material, representative of either moss or a gravely soil. We used average values for water retention parameters (α and n) from the van Genuchten model, while assigning high permeability and porosity. This allows the model to capture the key hydrological processes without overly specifying for either moss or gravely soil, thus providing flexibility in representing both substrate types.

Appendix B: Field observations

595 Qualitative observations in the field further include the seasonality of changes in saturation, visual interpretation of groundwater flow velocities using a dye tracer in the late thawing season in September 2022, and description of the soil material.

Due to snow- and pore ice melt in the early thawing season, the landscape in the sub-catchment is largely inundated as the active layer has only just started to develop and water can not infiltrate into the soil deeply yet. In the later season, the surface of the catchment is largely dry with a few highly saturated areas. Roughly in the middle of the catchment is a creek collecting

600 water from the catchment as well as from a perennial snow-patch at the catchment border.

Tracer tests with liquid Rhodamine and Fluorescein in September 2022 were used to qualitatively asses the order of magnitude of subsurface flow velocities. Tracers were injected at depths between 0.5 and 1.2 cm depth and at various distances (1, 5,

Figure B1. Rhodamine tracer emerging after several minutes from a subsurface seepage in the Endalen sub-catchment in September 2022 after injection at 2 m distance and ~ 0.5 m depth.

10, and 20 m) from a pond from which subsurface water was emerging below the ground surface (see Fig. B1). While the exact transport velocities and full BTC could not be determined, we observed a rapid initial breakthrough in the order of several minutes to several hours. This leads us to believe that the subsurface material is coarse (gravely) and allows for fast transport. The potential presence of preferential flow paths could not be determined.

The surface of the catchment is largely covered by mosses and short grasses, or by exposed gravel. The organic layer is not extensive and usually only reaches 2–10 cm deep based on spot samples and visual interpretation. Below, the gravely layer begins with an unknown depth and the stratification below these two layers cannot be determined.

Appendix C: Climate change scenario post-processing

To quantify mass transported from the injection location in the climate change scenarios, the visual output was used to extract the total solute mass from (1) the injection cell (in which the tracer has been injected in) and (2) the entire vertical column

in which the tracer was injected. Visual output from ATS contains values for all cells throughout the entire mesh for each time step of the simulation. We analyze the tracer mass integrated over the entire column due to the vertical tracer movements observed in Fig. 11. Visual output is available every 20 days throughout the simulation period. Despite a high output precision (1e-12), rounding and vertical integration leads to values higher than the initial injected mass (100 mol). Maximum values were 100.35 mol, 104.27 mol, and 100.65 mol in the columns for the RCP4.5, the RCP8.5, and the abrupt warming scenarios, respectively. For better visualization, solute mass values have been truncated to 100 in Fig. 10a and d, and Fig. 12a and b during the post-processing procedure.

Appendix D: Evaluation of Model Configuration

To ensure that our model results are not influenced by arbitrary choices regarding boundary conditions, parameters, or mesh discretization, we conducted a thorough assessment to evaluate the adequacy of these modeling decisions.

A domain depth of 40 m was selected to ensure that the depth of zero annual amplitude remains unaffected by the bottom boundary condition. As shown in Figure D1, the depth of zero annual amplitude is approximately 15 m. This demonstrates that the surface signal penetrates to this depth, beyond which interannual variations in surface forcing have negligible influence on ground temperatures.
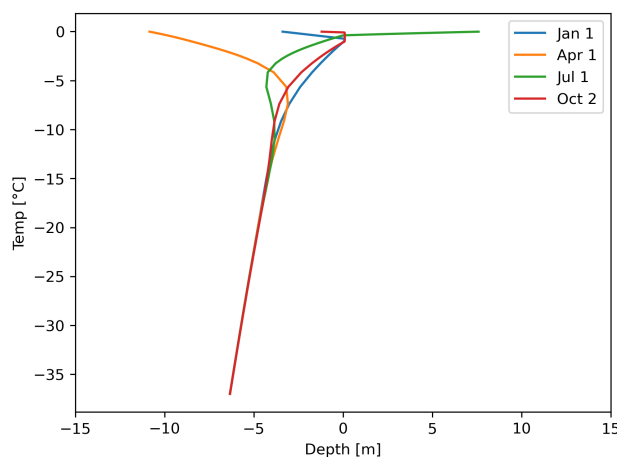
Figure D1. "Trumpet curves" showing the seasonal development of the soil temperature profile with depth for four given times. The profiles indicate that the zero annual amplitude depth is located at ∼15 m depth.

Furthermore, we demonstrate that a spinup time of ten years is sufficient by analyzing the day-of-year surface temperature differences between two consecutive years throughout the spinup period. As shown in Fig. D2, these differences are initially large (up to 4°C) but decrease steadily, becoming negligible by year five. After five years, the average difference throughout the year is less than 0.1°C, indicating that the system has reached a cyclic steady state.
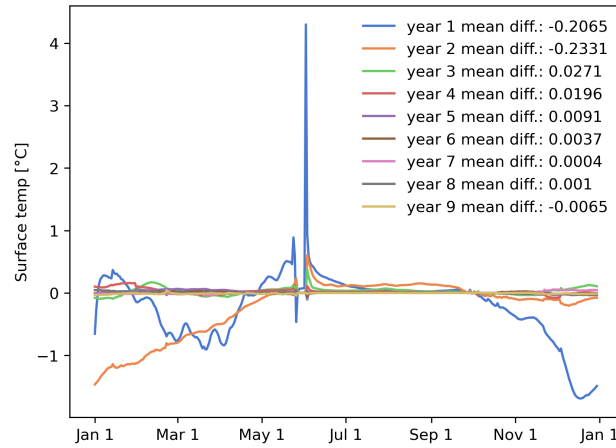
Figure D2. Surface temperature evolution in the region of interest throughout the spinup. The legend indicates the mean temperature difference throughout the year and suggests that after four years of spinup, the temperature differences are minimal with slight variations in daily absolute maximum differences. Overall, the temperature evolution shows that ten years of spinup are sufficient for this model setup.

For the climate change scenarios, air temperature was the only variable that changed and increased over time, while the bottom boundary temperature remained constant at -6°C throughout the 50-year simulation. To verify that this decision does not impact transport processes in the active layer, we conducted single 1D column simulations using the same forcing dataset but with two different bottom boundary conditions: (1) a constant temperature boundary condition and (2) a constant heat flux boundary condition. The results show that the choice of bottom boundary condition has minimal influence on the temperature and associated processes in the active layer during years 1–40 and only minor effects in years 40–50 (never exceeding a difference of one mesh cell). Therefore, we conclude that the constant temperature bottom boundary condition does not affect the results presented in Section 3.2.

In the mesh described in Appendix A, we chose to reduce the horizontal resolution in the upper slope area, which is not central to our study due to its low carbon content, but remains important for accurately representing the catchment hydrology. To evaluate effects of the mesh resolution, we ran three simulations with progressively increasing column widths in the upper slope area: the highest resolution used 5.8 m per column, the medium resolution had 12 m per column, and the lowest resolution used 23 m per column.

As shown in Fig D4, the mesh resolution in the upper slope area slightly influences the tracer breakthrough curves. We attribute these differences to how mesh resolution affects moisture transport and, consequently, the thaw rate. Faster thawing in the higher resolution cases, likely driven by differences in soil moisture, leads to earlier tracer release compared to the coarsest scenario. However, the overall travel times (short for buried carbon and prolonged for TOL carbon) are similar across the resolutions. For seasonal simulations of carbon transport, we opted for the finest resolution (5.8 m) in the upslope area, as it may most adequately capture the seasonal dynamics of thawing and solute transport.
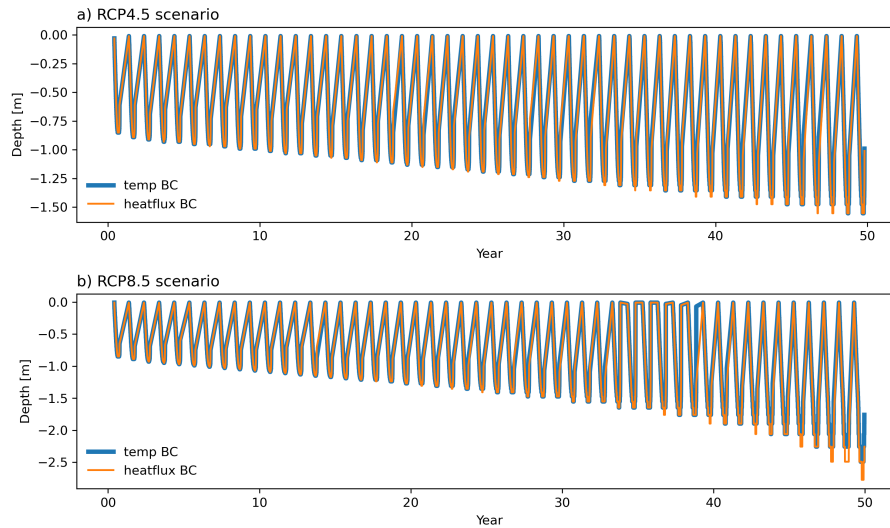
Figure D3. Thaw depth progression in simplified 1D column models using the same forcing as the full 2D transect in the main text for the (**a**) RCP 4.5 and (**b**) RCP 8.5 scenario, with each a constant temperature boundary condition (blue) and a heat flux boundary condition (orange) prescribed at the bottom of the domain.

650   A finer resolution leads to more responsive freeze-thaw and moisture release dynamics, causing slight differences in the active layer thaw rate, which leads to earlier tracer release compared to the coarsest resolution case. However, the relative differences in travel time behavior between TOL and buried carbon are similar across the various mesh resolution cases. For site-specific studies aiming to reproduce field measurements, accurate replication of field-measured thaw rates would be important. However, As the purpose of this study is to investigate relative effects of solute release in different depths, the

655   precise details of the thaw rates are not critical. Therefore, we decided to proceed with the coarsest mesh resolution for the climate change simulations, which are computationally more demanding due to the long simulation time (50 years).

Appendix E: Carbon distribution in Adventdalen, Svalbard

Slopes in the greater Adventdalen area are generally often characterized by the occurrence of solifluction processes. Solifluction can lead to the burial of organic matter into deeper soil layers, enriching the organic carbon content in samples taken from

660   different tributaries of the Adventdalen valley (such as the Endalen valley). Sampling soil cores in Adventdalen by Weiss et al. (2017) has revealed that SOC 0–100 cm stocks in solifluction affected areas are on average 20.7 kg C m^{-2}, which is much higher than the landscape-level mean of 4.2 kg C m^{-2} based on landform upscaling.

    Fig. E1 shows examples of four profiles from two solifluction areas in Adventdalen. The mean SOC 0–100 cm stock of these profiles is 23.4 kg C m^{-2}, slightly higher than the reported mean stock for solifluction areas reported in Weiss et al. (2017).

665   Profiles are generally deep before reaching bedrock or regolith (≥ 70 cm). They have a thin top organic layer (%C > 10)
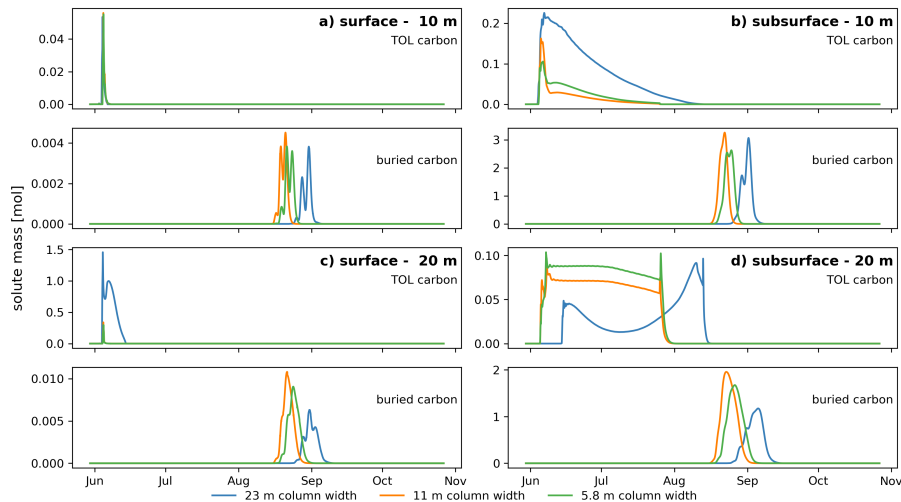
Figure D4. Breakthrough curves like shown in Fig. 5 without the surface transport contribution but including breakthrough curves for all tested mesh resolutions for the upper slope area. The different panels show breakthrough curves in the surface (a and c) and the subsurface (b and d) for each, the TOL carbon (top panel) and buried carbon (lower panel) for each of the three cases and at both observation point distances.

between 4.5–9 cm (mean 6.4 cm), which stores only 3.0–9.9% (mean 5.5%) of the total SOC stock in the top 100 cm of the profiles. The remainder is stored in the mineral active layer, with negligible amounts in the permafrost layer. Only in profile T3-1, the frost table was reached at 70 cm on the sampling date of July 1, 2013 but the active layer depth is certainly much deeper. Two profiles show some C-enrichment at greater depth, likely the result of burial by solifluction processes (T3-1 at
670   36–60 cm and T5-8 at 18–30 cm). T5 profiles have a larger volume of large stones in their profiles (up to 50%), which reduces total SOC 0–100 cm stocks compared to T3 profiles (no large stones, not shown).

Appendix F: Photogrammetry processing

After surveying the subcatchment in Endalen valley by drone, we process the survey in the photogrammetrical suite Agisoft Metashape version 1.8.4 using the default processing settings. We register the survey data to the 2009 Digital Elevation Model
675   (DEM) made by well-georeferenced aerial images by the Norwegian Polar Institute (Norwegian Polar Institute, 2014), using Iterative Closest Point (ICP) registration in CloudCompare version 2.12, leading to a mean vertical bias of 0.03 m, and a mean absolute point-to-point distance (which we consider the registration uncertainty) of 0.74 m. We assume minimal internal distortion in the survey due to the inclusion of oblique images (James et al., 2017) and therefore consider the affine transformation of the ICP registration sufficient for the accuracy that is required for the study. With a survey diameter of 990 m, this location
680   uncertainty is approximately equivalent to an angle uncertainty of 0.04° ($\tan^{-1} \frac{0.74}{990}$).
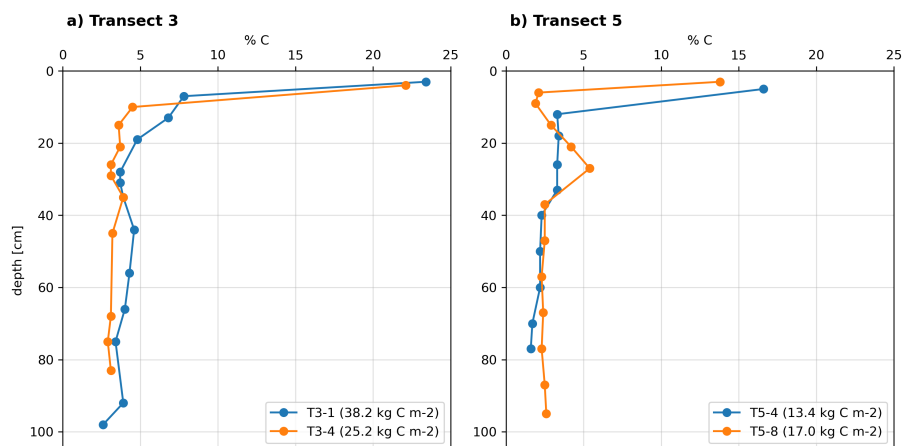
Figure E1. Organic carbon content (%) vs depth (cm) in four examples of soil profiles from the Adventdalen area. Transect 3 (**a**) is close to the Endalen valley, which represents the study site in this paper. Transect 5 (**b**) is located close to the Bolterdalen valley, ∼6.5 km southeast of the Endalen valley. Sampling depths vary depending on the sampling method and quality of the soil profiles retrieved. The total soil organic carbon storage in each profile is denoted in the legend entry next to the profile ID.

Author contributions. AH designed the study with help from AF, AAM, SLP, and EC. ESM surveyed the study site by drone and processed the digital elevation model. AH performed the model runs and analysis with help from AF, SLP, and EC. AH and AAM performed the post-processing of the model results to evaluate potential microbial mineralization rates. AH wrote the manuscript with contribution from all co-authors.

685 *Competing interests.* The authors declare that they have no conflict of interest.

Acknowledgements. Financial support for A.H. and A.F. for this research has been supported by the Svenska Forsknings-rådet Formas (grant no. 2017-00736) and by the Bolin Centre for Climate Research. Computations were enabled by resources provided by the National Academic Infrastructure for Supercomputing in Sweden (NAISS), partially funded by the Swedish Research Council through grant agreement no. 2022-06725. S.L.P and E.C. acknowledge support by the Next-Generation Ecosystem Experiment–Arctic (NGEE Arctic) project. The NGEE
690 Arctic project is supported by the Office of Biological and Environmental Research in the U.S. Department of Energy Office of Science. The authors also thank Peter Kuhry for providing us with field-based observations and measurements of carbon distributions in Adventdalen.

References

Abbott, B. W., Larouche, J. R., Jones, J. B., Bowden, W. B., and Balser, A. W.: Elevated dissolved organic carbon biodegradability from thawing and collapsing permafrost, Journal of Geophysical Research: Biogeosciences, 119, 2049–2063, https://doi.org/10.1002/2014JG002678, 2014.

Anderson, M. G. and Burt, T. P.: Toward more detailed field monitoring of variable source areas, Water Resources Research, 14, 1123–1131, https://doi.org/10.1029/WR014i006p01123, 1978.

Atchley, A. L., Painter, S. L., Harp, D. R., Coon, E. T., Wilson, C. J., Liljedahl, A. K., and Romanovsky, V. E.: Using field observations to inform thermal hydrology models of permafrost dynamics with ATS (v0.83), Geoscientific Model Development, 8, 2701–2722, https://doi.org/10.5194/gmd-8-2701-2015, 2015.

Bense, V. F., Ferguson, G., and Kooi, H.: Evolution of shallow groundwater flow systems in areas of degrading permafrost, Geophysical Research Letters, 36, L22 401, https://doi.org/10.1029/2009GL039225, 2009.

Bense, V. F., Kooi, H., Ferguson, G., and Read, T.: Permafrost degradation as a control on hydrogeological regime shifts in a warming climate, Journal of Geophysical Research: Earth Surface, 117, 2011JF002 143, https://doi.org/10.1029/2011JF002143, 2012.

Bowring, S. P. K., Lauerwald, R., Guenet, B., Zhu, D., Guimberteau, M., Tootchi, A., Ducharne, A., and Ciais, P.: ORCHIDEE MICT-LEAK (r5459), a global model for the production, transport, and transformation of dissolved organic carbon from Arctic permafrost regions – Part 1: Rationale, model description, and simulation protocol, Geoscientific Model Development, 12, 3503–3521, https://doi.org/10.5194/gmd-12-3503-2019, 2019.

Bowring, S. P. K., Lauerwald, R., Guenet, B., Zhu, D., Guimberteau, M., Regnier, P., Tootchi, A., Ducharne, A., and Ciais, P.: ORCHIDEE MICT-LEAK (r5459), a global model for the production, transport, and transformation of dissolved organic carbon from Arctic permafrost regions – Part 2: Model evaluation over the Lena River basin, Geoscientific Model Development, 13, 507–520, https://doi.org/10.5194/gmd-13-507-2020, 2020.

Christiansen, H. H., Gilbert, G. L., Demidov, N., Guglielmin, M., Isaksen, K., and Boike, J.: 10 Permafrost temperatures and active layer thickness in Svalbard during 2017/2018, https://doi.org/10.5281/zenodo.4777728, 2020.

Cole, J. J., Prairie, Y. T., Caraco, N. F., McDowell, W. H., Tranvik, L. J., Striegl, R. G., Duarte, C. M., Kortelainen, P., Downing, J. A., Middelburg, J. J., and Melack, J.: Plumbing the Global Carbon Cycle: Integrating Inland Waters into the Terrestrial Carbon Budget, Ecosystems, 10, 172–185, https://doi.org/10.1007/s10021-006-9013-8, 2007.

Connolly, C. T., Cardenas, M. B., Burkart, G. A., Spencer, R. G. M., and McClelland, J. W.: Groundwater as a major source of dissolved organic matter to Arctic coastal waters, Nature Communications, 11, 1479, https://doi.org/10.1038/s41467-020-15250-8, 2020.

Coon, E., Svyatsky, D., Jan, A., Kikinzon, E., Berndt, M., Atchley, A., Harp, D., Manzini, G., Shelef, E., Lipnikov, K., Garimella, R., Xu, C., Moulton, D., Karra, S., Painter, S., Jafarov, E., and Molins, S.: Advanced Terrestrial Simulator, https://doi.org/10.11578/DC.20190911.1, 2019.

Coon, E. T., David Moulton, J., and Painter, S. L.: Managing complexity in simulations of land surface and near-surface processes, Environmental Modelling & Software, 78, 134–149, https://doi.org/10.1016/j.envsoft.2015.12.017, 2016.

Dagenais, S., Molson, J., Lemieux, J.-M., Fortier, R., and Therrien, R.: Coupled cryo-hydrogeological modelling of permafrost dynamics near Umiujaq (Nunavik, Canada), Hydrogeology Journal, 28, 887–904, https://doi.org/10.1007/s10040-020-02111-3, 2020.

Denman, K. L., Brasseur, G., Chidthaisong, A., Ciais, P., Cox, P. M., Dickinson, R. E., Hauglustaine, D., Heinze, C., Holland, E., Jacob, D., Lohmann, U., Ramachandran, S., da Silva Dias, P. L., Wofsy, S. C., and Zhang, X.: Couplings Between Changes in the Climate System

and Biogeochemistry, in: Climate Change 2007: The Physical Science Basis. Contribution of Working Group I to the Fourth Assessment

730   Report of the Intergovernmental Panel on Climate Change, edited by Solomon, S., Qin, D., Manning, M., Chen, Z., Marquis, M., Averyt, K. B., Tignor, M., and Miller, H. L., pp. 499–587, Cambridge University Press, Cambridge, United Kingdom and New York, NY, USA, 2007.

Dunne, T. and Black, R. D.: An Experimental Investigation of Runoff Production in Permeable Soils, Water Resources Research, 6, 478–490, https://doi.org/10.1029/WR006i002p00478, 1970.

735   Dusek, J., Dohnal, M., Vogel, T., Marx, A., and Barth, J. A.: Modelling multiseasonal preferential transport of dissolved organic carbon in a shallow forest soil: Equilibrium versus kinetic sorption, Hydrological Processes, 33, 2898–2917, https://doi.org/10.1002/hyp.13536, 2019.

Fan, Y. and Bras, R. L.: Analytical solutions to hillslope subsurface storm flow and saturation overland flow, Water Resources Research, 34, 921–927, https://doi.org/10.1029/97WR03516, 1998.

740   Norwegian Polar Institue: Toposvalbard, https://toposvalbard.npolar.no/.

Frampton, A. and Destouni, G.: Impact of degrading permafrost on subsurface solute transport pathways and travel times, Water Resources Research, 51, 7680–7701, https://doi.org/10.1002/2014WR016689, 2015.

Frampton, A., Painter, S., Lyon, S. W., and Destouni, G.: Non-isothermal, three-phase simulations of near-surface flows in a model permafrost system under seasonal variability and climate change, Journal of Hydrology, 403, 352–359, https://doi.org/10.1016/j.jhydrol.2011.04.010,

745   2011.

Frampton, A., Painter, S. L., and Destouni, G.: Permafrost degradation and subsurface-flow changes caused by surface warming trends, Hydrogeology Journal, 21, 271–280, https://doi.org/10.1007/s10040-012-0938-z, 2013.

Gao, B. and Coon, E. T.: Evaluating simplifications of subsurface process representations for field-scale permafrost hydrology models, The Cryosphere, 16, 4141–4162, https://doi.org/10.5194/tc-16-4141-2022, 2022.

750   Ge, S., McKenzie, J., Voss, C., and Wu, Q.: Exchange of groundwater and surface-water mediated by permafrost response to seasonal and long term air temperature variation: GROUNDWATER AND PERMAFROST, Geophysical Research Letters, 38, n/a–n/a, https://doi.org/10.1029/2011GL047911, 2011.

Guimond, J. A., Mohammed, A. A., Walvoord, M. A., Bense, V. F., and Kurylyk, B. L.: Saltwater Intrusion Intensifies Coastal Permafrost Thaw, Geophysical Research Letters, 48, e2021GL094 776, https://doi.org/10.1029/2021GL094776, 2021.

755   Hamm, A. and Frampton, A.: Impact of lateral groundwater flow on hydrothermal conditions of the active layer in a high arctic hillslope setting, The Cryosphere, 15, 4853–4871, https://doi.org/10.5194/tc-2021-60, 2021.

Hanssen-Bauer, I., Førland, E., Hisdal, H., Mayer, S., Sandø, A., and Sorteberg, A.: Climate in Svalbard 2100 – a knowledge base for climate adaptation, Tech. Rep. 1/2019, Norwegian Centre for Climate Services, 2018.

Harp, D. R., Atchley, A. L., Painter, S. L., Coon, E. T., Wilson, C. J., Romanovsky, V. E., and Rowland, J. C.: Effect of soil property

760   uncertainties on permafrost thaw projections: a calibration-constrained analysis, The Cryosphere, 10, 341–358, https://doi.org/10.5194/tc-10-341-2016, 2016.

Hazenberg, P., Fang, Y., Broxton, P., Gochis, D., Niu, G., Pelletier, J. D., Troch, P. A., and Zeng, X.: A hybrid-3D hillslope hydrological model for use in E arth system models, Water Resources Research, 51, 8218–8239, https://doi.org/10.1002/2014WR016842, 2015.

765 Huang, X. and Rudolph, D. L.: Numerical Study of Coupled Water and Vapor Flow, Heat Transfer, and Solute Transport in Variably-Saturated Deformable Soil During Freeze-Thaw Cycles, Water Resources Research, 59, e2022WR032 146, https://doi.org/10.1029/2022WR032146, 2023.

Hugelius, G., Strauss, J., Zubrzycki, S., Harden, J. W., Schuur, E. A. G., Ping, C.-L., Schirrmeister, L., Grosse, G., Michaelson, G. J., Koven, C. D., O'Donnell, J. A., Elberling, B., Mishra, U., Camill, P., Yu, Z., Palmtag, J., and Kuhry, P.: Estimated stocks of circumpolar
770 permafrost carbon with quantified uncertainty ranges and identified data gaps, Biogeosciences, 11, 6573–6593, https://doi.org/10.5194/bg-11-6573-2014, 2014.

Intergovernmental Panel On Climate Change (IPCC): The Ocean and Cryosphere in a Changing Climate: Special Report of the Intergovernmental Panel on Climate Change, Cambridge University Press, 1 edn., ISBN 978-1-00-915796-4 978-1-00-915797-1, https://doi.org/10.1017/9781009157964, 2022.

775 Jafarov, E. E., Coon, E. T., Harp, D. R., Wilson, C. J., Painter, S. L., Atchley, A. L., and Romanovsky, V. E.: Modeling the role of preferential snow accumulation in through talik development and hillslope groundwater flow in a transitional permafrost landscape, Environmental Research Letters, 13, 105 006, https://doi.org/10.1088/1748-9326/aadd30, 2018.

Jafarov, E. E., Svyatsky, D., Newman, B., Harp, D., Moulton, D., and Wilson, C.: The importance of freeze–thaw cycles for lateral tracer transport in ice-wedge polygons, The Cryosphere, 16, 851–862, https://doi.org/10.5194/tc-16-851-2022, 2022.

780 James, M. R., Robson, S., and Smith, M. W.: 3-D uncertainty-based topographic change detection with structure-from-motion photogrammetry: precision maps for ground control and directly georeferenced surveys: 3-D uncertainty-based change detection for SfM surveys, Earth Surface Processes and Landforms, 42, 1769–1788, https://doi.org/10.1002/esp.4125, 2017.

Jan, A., Coon, E. T., and Painter, S. L.: Evaluating integrated surface/subsurface permafrost thermal hydrology models in ATS (v0.88) against observations from a polygonal tundra site, Geoscientific Model Development, 13, 2259–2276, https://doi.org/10.5194/gmd-13-2259-2020,
785 2020.

Kane, D. L., Yoshikawa, K., and McNamara, J. P.: Regional groundwater flow in an area mapped as continuous permafrost, NE Alaska (USA), Hydrogeology Journal, 21, 41–52, https://doi.org/10.1007/s10040-012-0937-0, 2013.

Kurylyk, B. L., Hayashi, M., Quinton, W. L., McKenzie, J. M., and Voss, C. I.: Influence of vertical and lateral heat transfer on permafrost thaw, peatland landscape transition, and groundwater flow: Permafrost thaw, landscape change and groundwater flow, Water Resources
790 Research, 52, 1286–1305, https://doi.org/10.1002/2015WR018057, 2016.

Lamontagne-Hallé, P., McKenzie, J. M., Kurylyk, B. L., and Zipper, S. C.: Changing groundwater discharge dynamics in permafrost regions, Environmental Research Letters, 13, 084 017, https://doi.org/10.1088/1748-9326/aad404, 2018.

Langer, M., von Deimling, T. S., Westermann, S., Rolph, R., Rutte, R., Antonova, S., Rachold, V., Schultz, M., Oehme, A., and Grosse, G.: Thawing permafrost poses environmental threat to thousands of sites with legacy industrial contamination, Nature Communications, 14,
795 1721, https://doi.org/10.1038/s41467-023-37276-4, 2023.

Lapalme, C. M., Spence, C., Costa, D., Bonsal, B. R., Musetta-Lambert, J., and Fazli, Y.: Towards the incorporation of hydrogeochemistry into the modelling of permafrost environments: a review of recent recommendations, considerations, and literature, Arctic Science, pp. as–2022–0038, https://doi.org/10.1139/as-2022-0038, 2023.

Lemieux, J., Frampton, A., and Fortier, P.: Recent Advances (2018–2023) and Research Opportunities in the Study of Groundwater in Cold
800 Regions, Permafrost and Periglacial Processes, p. ppp.2255, https://doi.org/10.1002/ppp.2255, 2024.

Magnússon, R. Í., Hamm, A., Karsanaev, S. V., Limpens, J., Kleijn, D., Frampton, A., Maximov, T. C., and Heijmans, M. M. P. D.: Extremely wet summer events enhance permafrost thaw for multiple years in Siberian tundra, Nature Communications, 13, 1556, https://doi.org/10.1038/s41467-022-29248-x, 2022.

McKenzie, J. M., Voss, C. I., and Siegel, D. I.: Groundwater flow with energy transport and water–ice phase change: Numerical simulations, benchmarks, and application to freezing in peat bogs, Advances in Water Resources, 30, 966–983, https://doi.org/10.1016/j.advwatres.2006.08.008, 2007.

Miner, K. R., D'Andrilli, J., Mackelprang, R., Edwards, A., Malaska, M. J., Waldrop, M. P., and Miller, C. E.: Emergent biogeochemical risks from Arctic permafrost degradation, Nature Climate Change, 11, 809–819, https://doi.org/10.1038/s41558-021-01162-y, 2021.

Miner, K. R., Turetsky, M. R., Malina, E., Bartsch, A., Tamminen, J., McGuire, A. D., Fix, A., Sweeney, C., Elder, C. D., and Miller, C. E.: Permafrost carbon emissions in a changing Arctic, Nature Reviews Earth & Environment, 3, 55–67, https://doi.org/10.1038/s43017-021-00230-3, 2022.

Mohammed, A. A., Bense, V. F., Kurylyk, B. L., Jamieson, R. C., Johnston, L. H., and Jackson, A. J.: Modeling Reactive Solute Transport in Permafrost-Affected Groundwater Systems, Water Resources Research, 57, https://doi.org/10.1029/2020WR028771, 2021.

Mohammed, A. A., Guimond, J., Bense, V., Jamieson, R., McKenzie, J. M., and Kurylyk, B.: Mobilization of subsurface carbon pools driven by permafrost thaw and reactivation of groundwater flow: a virtual experiment, Environmental Research Letters, https://doi.org/10.1088/1748-9326/aca701, 2022.

Molins, S., Svyatsky, D., Xu, Z., Coon, E. T., and Moulton, J. D.: A multicomponent reactive transport model for integrated surface-subsurface hydrology problems, Water Resources Research, 58, https://doi.org/10.1029/2022WR032074, 2022.

Mutschlecner, A. E., Guerard, J. J., Jones, J. B., and Harms, T. K.: Regional and intra-annual stability of dissolved organic matter composition and biolability in high-latitude Alaskan rivers, Limnology and Oceanography, 63, 1605–1621, https://doi.org/10.1002/lno.10795, 2018.

Norwegian Climate Service Centre: Longyearbyen airport weather data, https://klimaservicesenter.no/, last access: July 2022, 2023.

Norwegian Polar Institute: Terrengmodell Svalbard (S0 Terrengmodell), https://doi.org/10.21334/npolar.2014.dce53a47, type: dataset, 2014.

O'Donnell, J. A., Aiken, G. R., Walvoord, M. A., and Butler, K. D.: Dissolved organic matter composition of winter flow in the Yukon River basin: Implications of permafrost thaw and increased groundwater discharge, Global Biogeochemical Cycles, 26, 2012GB004 341, https://doi.org/10.1029/2012GB004341, 2012.

Painter, S. L., Coon, E. T., Atchley, A. L., Berndt, M., Garimella, R., Moulton, J. D., Svyatskiy, D., and Wilson, C. J.: Integrated surface/subsurface permafrost thermal hydrology: Model formulation and proof-of-concept simulations, Water Resources Research, 52, 6062–6077, https://doi.org/10.1002/2015WR018427, 2016.

Painter, S. L., Coon, E. T., Khattak, A. J., and Jastrow, J. D.: Drying of tundra landscapes will limit subsidence-induced acceleration of permafrost thaw, Proceedings of the National Academy of Sciences, 120, e2212171 120, https://doi.org/10.1073/pnas.2212171120, 2023.

Paniconi, C., Troch, P. A., Van Loon, E. E., and Hilberts, A. G. J.: Hillslope-storage Boussinesq model for subsurface flow and variable source areas along complex hillslopes: 2. Intercomparison with a three-dimensional Richards equation model, Water Resources Research, 39, 2002WR001 730, https://doi.org/10.1029/2002WR001730, 2003.

Plaza, C., Pegoraro, E., Bracho, R., Celis, G., Crummer, K. G., Hutchings, J. A., Hicks Pries, C. E., Mauritz, M., Natali, S. M., Salmon, V. G., Schädel, C., Webb, E. E., and Schuur, E. A. G.: Direct observation of permafrost degradation and rapid soil carbon loss in tundra, Nature Geoscience, 12, 627–631, https://doi.org/10.1038/s41561-019-0387-6, 2019.

Rawlins, M. A., Connolly, C. T., and McClelland, J. W.: Modeling Terrestrial Dissolved Organic Carbon Loading to Western Arctic Rivers, Journal of Geophysical Research: Biogeosciences, 126, e2021JG006 420, https://doi.org/10.1029/2021JG006420, 2021.

Schuster, P. F., Schaefer, K. M., Aiken, G. R., Antweiler, R. C., Dewild, J. F., Gryziec, J. D., Gusmeroli, A., Hugelius, G., Jafarov, E., Krabben-
hoft, D. P., Liu, L., Herman-Mercer, N., Mu, C., Roth, D. A., Schaefer, T., Striegl, R. G., Wickland, K. P., and Zhang, T.: Permafrost Stores
a Globally Significant Amount of Mercury, Geophysical Research Letters, 45, 1463–1471, https://doi.org/10.1002/2017GL075571, 2018.

Schuur, E. A. G., McGuire, A. D., Schädel, C., Grosse, G., Harden, J. W., Hayes, D. J., Hugelius, G., Koven, C. D., Kuhry, P., Lawrence,
D. M., Natali, S. M., Olefeldt, D., Romanovsky, V. E., Schaefer, K., Turetsky, M. R., Treat, C. C., and Vonk, J. E.: Climate change and the
permafrost carbon feedback, Nature, 520, 171–179, https://doi.org/10.1038/nature14338, 2015.

Schytt Mannerfelt, E.: UAV survey images of the eastern Endalen slope, Svalbard, https://doi.org/10.5281/zenodo.8279263, 2023.

Semiletov, I., Pipko, I., Gustafsson, , Anderson, L. G., Sergienko, V., Pugach, S., Dudarev, O., Charkin, A., Gukov, A., Bröder, L., Andersson,
A., Spivak, E., and Shakhova, N.: Acidification of East Siberian Arctic Shelf waters through addition of freshwater and terrestrial carbon,
Nature Geoscience, 9, 361–365, https://doi.org/10.1038/ngeo2695, 2016.

Shojae Ghias, M., Therrien, R., Molson, J., and Lemieux, J.-M.: Numerical simulations of shallow groundwater flow and heat transport in
continuous permafrost setting under impact of climate warming, Canadian Geotechnical Journal, 56, 436–448, https://doi.org/10.1139/cgj-
2017-0182, 2019.

Siewert, M. B., Hanisch, J., Weiss, N., Kuhry, P., Maximov, T. C., and Hugelius, G.: Comparing carbon storage of Siberian tundra
and taiga permafrost ecosystems at very high spatial resolution, Journal of Geophysical Research: Biogeosciences, 120, 1973–1994,
https://doi.org/10.1002/2015JG002999, 2015.

Sjöberg, Y., Jan, A., Painter, S. L., Coon, E. T., Carey, M. P., O'Donnell, J. A., and Koch, J. C.: Permafrost Promotes Shallow Groundwater
Flow and Warmer Headwater Streams, Water Resources Research, 57, https://doi.org/10.1029/2020WR027463, 2021.

Smith, M. I., Ke, Y., Geyman, E. C., Reahl, J. N., Douglas, M. M., Seelen, E. A., Magyar, J. S., Dunne, K. B. J., Mutter, E. A., Fischer,
W. W., Lamb, M. P., and West, A. J.: Mercury stocks in discontinuous permafrost and their mobilization by river migration in the Yukon
River Basin, Environmental Research Letters, 19, 084 041, https://doi.org/10.1088/1748-9326/ad536e, 2024.

Strand, S. M., Christiansen, H. H., Johansson, M., Åkerman, J., and Humlum, O.: Active layer thickening and controls on in-
terannual variability in the Nordic Arctic compared to the circum-Arctic, Permafrost and Periglacial Processes, p. ppp.2088,
https://doi.org/10.1002/ppp.2088, 2020.

Tarnocai, C., Canadell, J. G., Schuur, E. A. G., Kuhry, P., Mazhitova, G., and Zimov, S.: Soil organic carbon pools in the northern circumpolar
permafrost region, Global Biogeochemical Cycles, 23, n/a–n/a, https://doi.org/10.1029/2008GB003327, 2009.

The University Centre in Svalbard: Adventdalen weather data, https://www.unis.no/facilities/weather-stations/, last access: July 2022, 2023.

Troch, P. A., Paniconi, C., and Emiel Van Loon, E.: Hillslope-storage Boussinesq model for subsurface flow and variable source
areas along complex hillslopes: 1. Formulation and characteristic response, Water Resources Research, 39, 2002WR001 728,
https://doi.org/10.1029/2002WR001728, 2003.

Wales, N. A., Gomez-Velez, J. D., Newman, B. D., Wilson, C. J., Dafflon, B., Kneafsey, T. J., Soom, F., and Wullschleger, S. D.: Understand-
ing the relative importance of vertical and horizontal flow in ice-wedge polygons, Hydrology and Earth System Sciences, 24, 1109–1129,
https://doi.org/10.5194/hess-24-1109-2020, 2020.

Walvoord, M. A. and Kurylyk, B. L.: Hydrologic Impacts of Thawing Permafrost—A Review, Vadose Zone Journal, 15, 0,
https://doi.org/10.2136/vzj2016.01.0010, 2016.

Weiss, N., Faucherre, S., Lampiris, N., and Wojcik, R.: Elevation-based upscaling of organic carbon stocks in High-
Arctic permafrost terrain: a storage and distribution assessment for Spitsbergen, Svalbard, Polar Research, 36, 1400 363,
https://doi.org/10.1080/17518369.2017.1400363, 2017.

Wen, H., Perdrial, J., Abbott, B. W., Bernal, S., Dupas, R., Godsey, S. E., Harpold, A., Rizzo, D., Underwood, K., Adler, T., Sterle, G., and Li, L.: Temperature controls production but hydrology regulates export of dissolved organic carbon at the catchment scale, Hydrology and Earth System Sciences, 24, 945–966, https://doi.org/10.5194/hess-24-945-2020, 2020.

880 Wild, B., Andersson, A., Bröder, L., Vonk, J., Hugelius, G., McClelland, J. W., Song, W., Raymond, P. A., and Gustafsson, Ö.: Rivers across the Siberian Arctic unearth the patterns of carbon release from thawing permafrost, Proceedings of the National Academy of Sciences, 116, 10 280–10 285, https://doi.org/10.1073/pnas.1811797116, 2019.

Wu, R., Trubl, G., Taş, N., and Jansson, J. K.: Permafrost as a potential pathogen reservoir, One Earth, 5, 351–360, https://doi.org/10.1016/j.oneear.2022.03.010, 2022.

885 Yurova, A., Sirin, A., Buffam, I., Bishop, K., and Laudon, H.: Modeling the dissolved organic carbon output from a boreal mire using the convection-dispersion equation: Importance of representing sorption: MODELING DOC OUTPUT FROM A BOREAL MIRE, Water Resources Research, 44, https://doi.org/10.1029/2007WR006523, 2008.

Zastruzny, S. F., Sjöberg, Y., Jensen, K. H., Liu, Y., and Elberling, B.: Impact of Summer Air Temperature on Water and Solute Transport on a Permafrost-Affected Slope in West Greenland, Water Resources Research, 60, e2023WR036 147,

890 https://doi.org/10.1029/2023WR036147, 2024.

Zimov, S. A., Schuur, E. A. G., and Chapin, F. S.: Permafrost and the Global Carbon Budget, Science, 312, 1612–1613, https://doi.org/10.1126/science.1128908, 2006.